Vascular Segmentation of Phase Contrast Magnetic Resonance Angiograms Based on Statistical Mixture Modeling and Local Phase Coherence

Albert C. S. Chung*, J. Alison Noble, *Member, IEEE*, and Paul Summers

***Abstract*—In this paper, we present an approach to segmenting the brain vasculature in phase contrast magnetic resonance angiography (PC-MRA). According to our prior work, we can describe the overall probability density function of a PC-MRA speed image as either a Maxwell-uniform (MU) or Maxwell-Gaussian-uniform (MGU) mixture model. An automatic mechanism based on Kullback–Leibler divergence is proposed for selecting between the MGU and MU models given a speed image volume. A coherence measure, namely local phase coherence (LPC), which incorporates information about the spatial relationships between neighboring flow vectors, is defined and shown to be more robust to noise than previously described coherence measures. A statistical measure from the speed images and the LPC measure from the phase images are combined in a probabilistic framework, based on the maximum *a posteriori* method and Markov random fields, to estimate the posterior probabilities of vessel and background for classification. It is shown that segmentation based on both measures gives a more accurate segmentation than using either speed or flow coherence information alone. The proposed method is tested on synthetic, flow phantom and clinical datasets. The results show that the method can segment normal vessels and vascular regions with relatively low flow rate and low signal-to-noise ratio, e.g., aneurysms and veins.**

***Index Terms*—Image segmentation, Kullback–Leibler divergence (KLD), local phase coherence, magnetic resonance angiography (MRA), Markov random fields (MRF).**

I. Introduction

MAGNETIC RESONANCE angiography (MRA) is a collection of noninvasive and flow-dependent methods for three-dimensional (3-D) vessel delineation that has the advantage of not relying on ionizing radiation. In this paper, we propose an automatic statistical method for segmenting brain vessels in phase contrast (PC) MRA images. Three-dimensional vascular segmentation is extremely useful for diagnosis and endovascular treatments of arterial diseases because it provides interventional radiologists with 3-D shape and structural information of the vessels of interest.

Manuscript received October 30, 2003; revised August 15, 2004. The work of A. C. S. Chung was supported by the Research Grants Council of Hong Kong under Grant HKUST6209/02E, Grant DAG01/02.EG04, and Grant HIA01/02.EG03. The Associate Editor responsible for coordinating the review of this paper and recommending its publication was Z.-P. Liang. *Asterisk indicates corresponding author.*

*A. C. S. Chung is with the Department of Computer Science, the Hong Kong University of Science and Technology, Clear Water Bay, Hong Kong (e-mail: achung@cs.ust.hk).

J. A. Noble is with the Medical Vision Laboratory, Department of Engineering Science, The University of Oxford, Oxford OX1 3PJ, U.K.

P. Summers is with the Institute of Neuroradiology, University Hospital Zurich, 8091, Zurich, Switzerland.

Digital Object Identifier 10.1109/TMI.2004.836877

Statistical mixture models have been employed in segmentation of magnetic resonance and computed tomographic images, e.g., [1]–[7]. In Wilson and Noble [8] a statistical mixture model in segmenting time-of-flight (TOF) MRA images for the visualization of brain vessels. Similarly, we propose a statistical mixture model to describe background and vascular signals in PC-MRA speed images. Based on the formation of PC-MRA speed images and the physical properties of blood flow, we assume that the probability density functions (pdfs) of background and vascular signals can be modeled by the Maxwell distribution and uniform distribution, respectively [9], [10].

As will be discussed in Section II, in some cases, the mixture distribution may not perfectly fit the observed speed image histogram. To accommodate this, the modeling of an observed speed image pdf can be improved by adding a Gaussian component [11] and, thus, approximated by a linear mixture of a Maxwell, Gaussian, and uniform distribution, namely a Maxwell-Gaussian-uniform (MGU) mixture model. In this paper, given a speed image histogram and the fitted MGU and MU mixture models, we propose an information theoretic mechanism for automatically selecting between these models.

A variety of approaches have been proposed for the segmentation of intracranial vasculature in speed images. For instance, Mclnerney *et al.* proposed topologically adaptable surfaces (T-surfaces), a variant of the classical deformable models with an efficient topologically adaptable property [12]. Another variant, geodesic active contours, was proposed by Lorigo *et al.* [13]. A fast vessel delineation method was introduced by Wink *et al.* to iteratively reconstruct a vessel segment defined by two user-specified starting and end points [14]. Krissian *et al.* [15] proposed a multiscale method to detect the vessel centerline and estimate vessel width based on eigenvalue and eigenvector analysis of the Hessian matrix, which relies on the partial differentiation in the speed images. In all of these methods, an intensity-based gradient function was employed to give information about the boundaries of vessels. A drawback in using a gradient-based method is that, in practice, gradient values are often not sufficiently high in the low flow regions for satisfactory segmentation. While most of the arterial anatomy can be seen clearly in speed images, gradient-based methods are generally not applicable to the segmentation of aneurysms and veins. These can contain low or complex flow leading to low signal-to-noise ratio (SNR) in speed images through the small resulting phase shifts, or cancellation of signals on summation of the contributing vectors [16], [17]. Where the resulting vascular signal approximates that of the background, these inhomogeneous subregions make vascular segmentation difficult.

PC-MRA images, which give high contrast between background and vascular regions [18], are often used for the visualization of brain vessels and related malformations, e.g., aneurysms. The main advantage of PC-MRA over other MRA methods is that, in addition to a speed-dependent image, it measures the x, y, and z velocity components of the flow vectors on a voxel-by-voxel basis, and provides velocity field information about the motion of blood in the brain. Each component of the flow vector is directly mapped onto the phase shift induced by the dephasing and partial rephasing of moving spins under the influence of a bipolar gradient used to encode velocity in phase contrast sequences [18]. Four data volumes, including three phase shift values (representing the velocity components) and speed (or flow magnitude) image, are obtained after the scanning. The focus of this work is to demonstrate that flow coherence information, which is extracted from the flow velocity field in a PC-MRA dataset, can be combined with the speed information to detect and segment both normal brain vessels, and regions with relatively low signal-to-noise and low flow rate, e.g., aneurysms and veins.

The rest of the paper is organized in the following way: Section II describes the statistical modeling of PC-MRA speed images and presents a new model selection mechanism. Section III gives the background of related coherence measures and formally defines the local phase coherence (LPC) measure. Section IV derives a probabilistic framework for combining speed information and flow coherence measures. Section V describes the experiments and results. Section VI concludes the paper.

II. Statistical Modelling of PC-MRA Speed Images and Model Selection Mechanism

Following the formalism laid out in our prior work [9], we describe the overall pdf of a PC-MRA speed image as either a Maxwell-uniform (MU) or MGU mixture model. With i representing the image intensity value, the pdfs $f(i)$ for these models are given by

MU model:

and
$$f_{\mathrm{MU}}(i) = w_M f_M(i) + w_U f_U(i) \tag{1}$$

MGU model:

$$f_{\mathrm{MGU}}(i) = w_M f_M(i) + w_G f_G(i) + w_U f_U(i) \tag{2}$$

respectively. They are also called finite mixture models [11]. In these expressions, the constituent Maxwell distribution has the form

$$f_M(i) = \sqrt{\frac{2}{\pi}} \cdot \frac{i^2}{\sigma_M^3} \cdot e^{\left(\frac{-i^2}{2\sigma_M^2}\right)} \tag{3}$$

where σ_M represents the distribution standard deviation, $i \geq 0$, and $f_M(i) = 0$ when $i < 0$. While the Gaussian distribution is given by

$$f_G(i) = \frac{1}{\sqrt{2\pi}\sigma_G} \cdot e^{\frac{-(i-\mu_G)^2}{2\sigma_G^2}} \tag{4}$$

where μ_G and σ_G^2 are the mean and variance of the Gaussian distribution, respectively, the uniform distribution is expressed as

$$f_U(i) = \frac{1}{I_{\max}} \tag{5}$$

where $I_{\max}$ is the maximum intensity in the observed frequency histogram. The combination of these distributions in (1) and (2) is subject to the weights w_M, w_G, and w_U, where $0 \leq w_M$, w_G, $w_U \leq 1$, and weights sum to one in each equation. The expectation-maximization (EM) algorithm is employed to estimate the parameters by maximizing the log-likelihood of the mixture distribution [19]. The update equations of the EM algorithm and implementation details can be found in [9] and [10].

Fig. 1 shows a maximum intensity projection (MIP) of a PC-MRA volume, an intensity histogram of the volume (solid line), and the fitted MU mixture distribution (dotted line) by using the EM-based parameter estimation algorithm. As shown in Fig. 1(b), the MU mixture distribution provides a good approximation of the observed intensity histogram. According to the maximum *a posteriori* (MAP) criterion, the image threshold I_{MU} is defined as the intersection of the Maxwell and uniform distributions, i.e., $w_M f_M(I_{\mathrm{MU}}) = w_U f_U(I_{\mathrm{MU}})$, as indicated in the figure. One of the speed images in the volume is shown in Fig. 1(c). Based on the estimated threshold I_{MU}, Fig. 1(d) shows its corresponding binary segmented image.

In addition, we have found that, due to vessels of subvoxel size, relatively low flow rates in some arteries and veins, slight tissue motion and ghosting artefacts, the mixture distribution may not perfectly fit the observed PC-MRA speed image histogram. To accommodate this, the modeling can be improved by adding a Gaussian component [9], [10]. Therefore, we approximate the observed image pdf by a linear mixture of a Maxwell distribution, a Gaussian distribution and a uniform distribution, as given in (2). The pdf becomes a MGU mixture model $f_{\mathrm{MGU}}(i)$.

For illustration, Fig. 2(a) shows a MIP of a second PC-MRA volume. Fig. 2(b) and (c) plots the fitted MU and MGU mixture distributions, respectively, and illustrate that the MGU mixture distribution gives a better representation of the observed intensity histogram than the MU mixture distribution in this situation, and that the added Gaussian component improves the description of the intensity histogram. Similarly, according to the MAP criterion, the image threshold I_{MGU} is defined as the intersection of the Maxwell-Gaussian and uniform distributions, i.e., $w_M f_M(I_{\mathrm{MGU}}) + w_G f_G(I_{\mathrm{MGU}}) = w_U f_U(I_{\mathrm{MGU}})$, and is indicated in Fig. 2(c). The estimated Maxwell and Gaussian distributions are plotted in Fig. 2(d). Note that the intersection between Maxwell and Gaussian distributions is not used as an image threshold because, in general, the threshold is too low and results in an excess of background pixels being identified as vessels. A segmented image, as shown in Fig. 2(f), was obtained from one of the speed images in the volume [Fig. 2(e)] based on the estimated threshold I_{MGU}. As compared with another segmented image based on a threshold I_{MU} [Fig. 2(g)], the use of the MGU model could lead to a better estimation of image threshold because there are fewer noisy pixels.

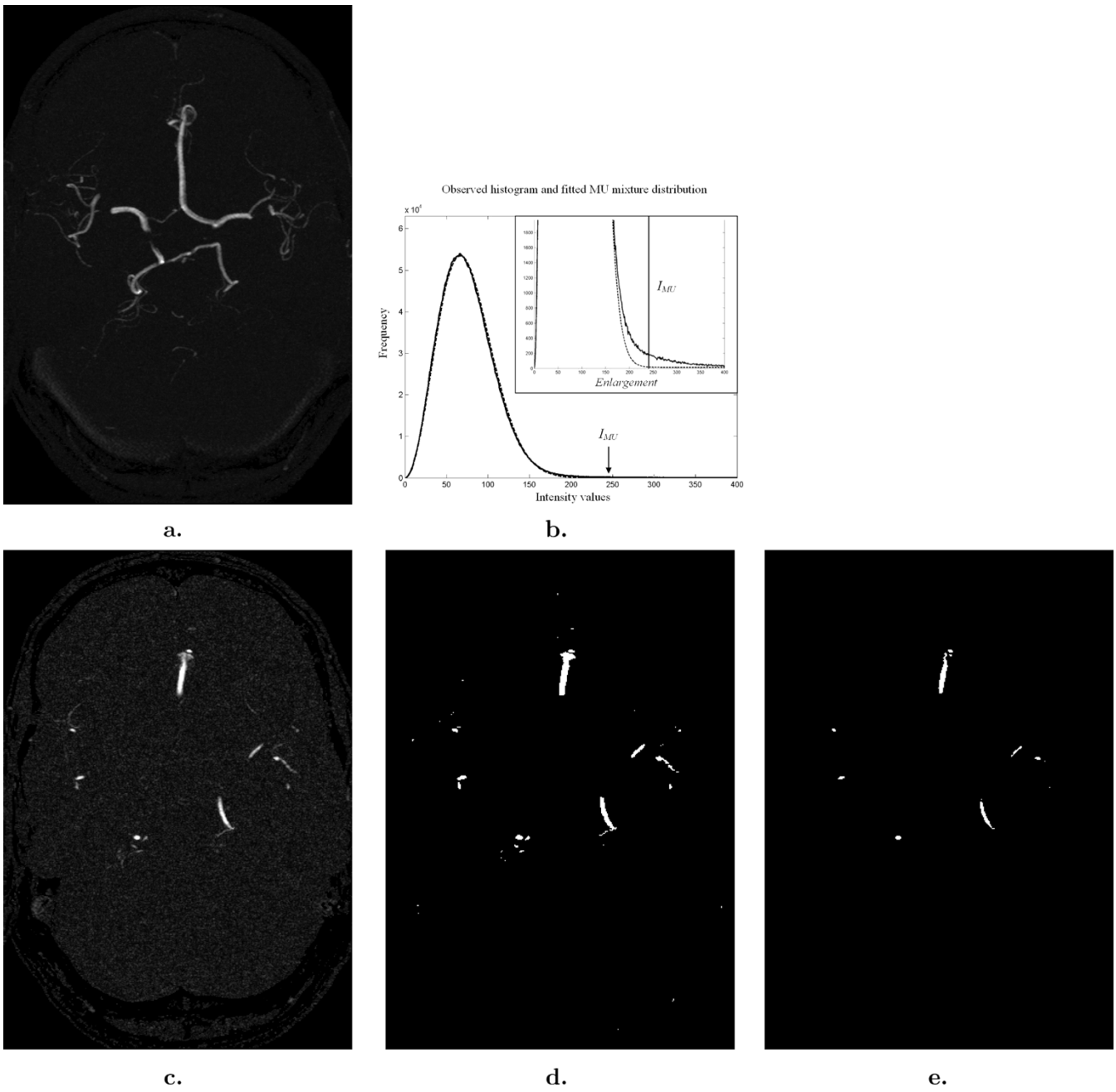

Fig. 1. Demonstration of the failure of the MGU mixture model to improve on the MU model when segmenting a PC-MRA image volume. (a) A MIP of a PC-MRA speed image volume. (b) An intensity histogram of the volume (solid line), and the fitted MU mixture distribution (dotted line) by using the EM-based parameter estimation algorithm (The vertical axis ranges from 0 to 6×10^4). The insert is an enlargement of the histogram (The vertical axis ranges from 0 to 1800). (c) One of speed images in the volume. (d) Segmented image of (c) based on a threshold, $I_{\mathrm{MU}} = 248$, estimated by using the fitted MU model. (e) For comparison, it shows a segmented image of (c) based on a threshold, $I_{\mathrm{MGU}} = 475$, estimated by using the fitted MGU model which gives an excessively high estimate for the image threshold and a suboptimal segmentation.

We have noted, however, that when the MU mixture distribution approximates the observed intensity histogram well, the Gaussian component of the MGU mixture model has a relatively large variance. This flattened Gaussian component may lead to an excessively high estimate for the image threshold I_{MGU}, and a suboptimal segmentation, as shown in Fig. 1(e). In this paper, we propose a new information theoretic procedure to choose between the MGU and MU models for each PC-MRA speed image volume. Given an observed histogram, let the fitted MGU and MU models be $f_{\mathrm{MGU}}(i) = w'_M f'_M(i) + w'_G f'_G(i) + w'_U f'_U(i)$ and $f_{\mathrm{MU}}(i) = w_M f_M(i) + w_U f_U(i)$, respectively. We define two measures J_1 and J_2 based on the Kullback–Leibler divergence (KLD) J, which is a symmetric version of the Kullback–Leibler distance and is widely used for measuring the difference between two distributions [20]. They are given by

$$J_1\left(w'_M f'_M + w'_G f'_G \| w_M f_M\right) \quad \text{and} \quad J_2\left(w'_M f'_M \| w_M f_M\right) \tag{6}$$

where $J(p\|q) = \sum_i (p(i) - q(i)) \log(p(i)/q(i))$, for any distributions p and q, and $J = 0$ when $p = q$.

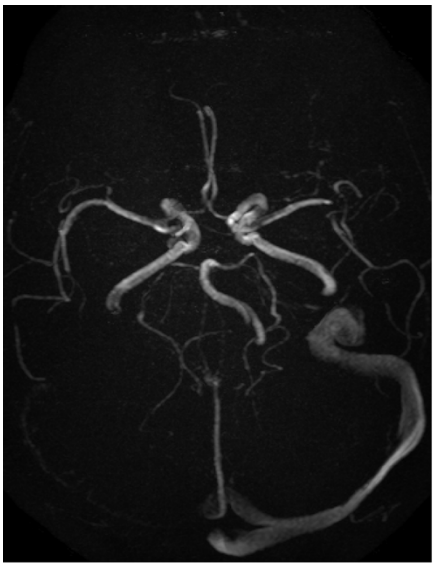

a.

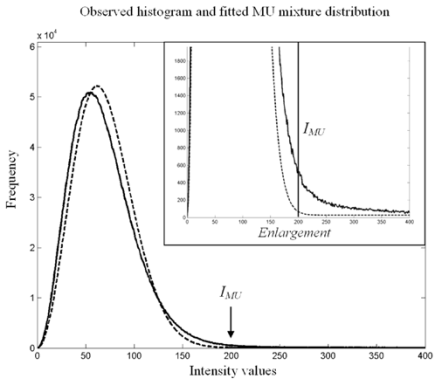

b.

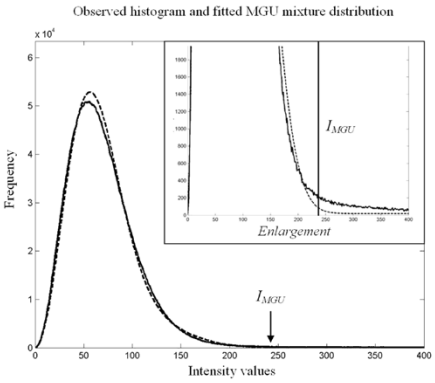

c.

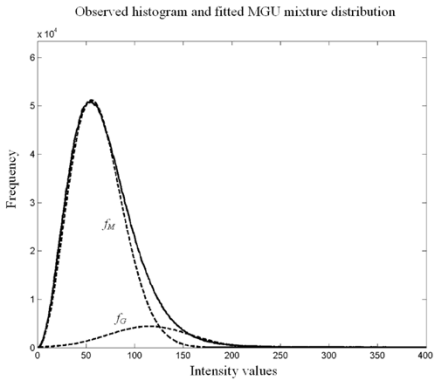

d.

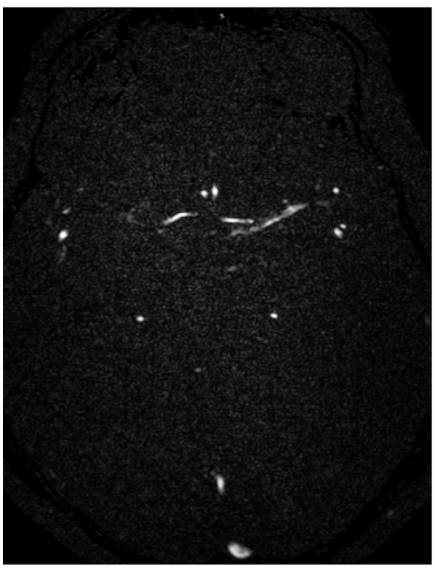

e.

f.

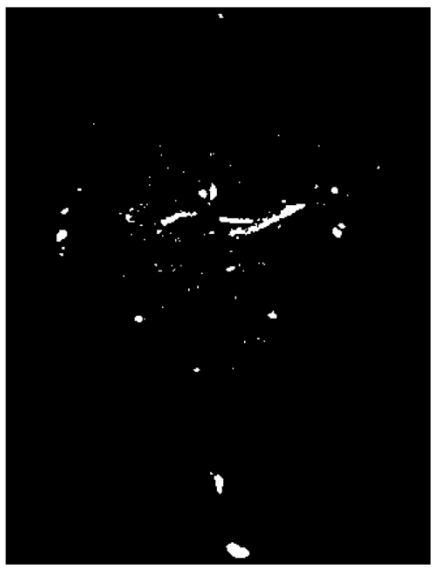

g.

Fig. 2. An example of improvement on the MU model by using the MGU model to achieve improved segmentation, in particular, note the reduction in the number of false-positive vessel identifications (small points). (a) A MIP of a PC-MRA speed image volume. (b) An intensity histogram (solid line), and the fitted MU mixture distribution (dotted line). The vertical axis ranges from 0 to 6×10^4. (c) The fitted MGU mixture distribution. The inserts are the histogram enlargements (The vertical axes range from 0 to 1800). (d) The fitted individual distributions: f_M and f_G (dotted lines). (e) One of speed images in the volume. (f) Segmented image of (e) based on a threshold, $I_{\mathrm{MGU}} = 241$. (g) Segmented image of (e) based on a threshold, $I_{\mathrm{MU}} = 201$.

When the MU model f_{MU} fits well to the observed intensity histogram $h(i)$ [see Fig. 1(b)], the added Gaussian component $w'_G f'_G$ in the MGU model f_{MGU} tends to have relatively large variance and shift to the high intensity range in the histogram. This causes the estimated threshold I_{MGU} to become relatively high, as shown in Fig. 1(e). The image can then be under-segmented. The Maxwell distributions in the MGU and MU models, $w'_M f'_M$ and $w_M f_M$, respectively, should be roughly the same. As such, $J_2(w'_M f'_M || w_M f_M) < J_1(w'_M f'_M + w'_G f'_G || w_M f_M)$.

Conversely, when the MU model f_{MU} does not fit well to the observed intensity histogram [see Fig. 2(b)], the added Gaussian component $w'_G f'_G$ in the fitted MGU model f_{MGU} is likely to have relatively small variance, and be shifted to the low intensity region in the histogram [see Fig. 2(c) and (d)]. As such, there should be a relatively small discrepancy between the Maxwell-Gaussian distribution in the MGU model and Maxwell distribution in the MU model. Therefore, $J_1(w'_M f'_M + w'_G f'_G || w_M f_M) < J_2(w'_M f'_M || w_M f_M)$.

These observations lead to a procedure for choosing between MGU and MU models whereby the MU model will be selected if J_1 is larger than J_2, and the MGU model will be selected if J_1 is smaller than J_2. Either of the MGU or MU models may be selected when $J_1 = J_2$.

III. Local Phase Coherence (LPC) Measure

In this section, we formally introduce a coherence measure to quantify locally coherent flow patterns. This coherence measure is named the local phase coherence (LPC), and is very helpful in distinguishing locally coherent flow fields from (noncoherent) random flow fields. Conceptually, LPC treats the coherence and random flow patterns as regions of texture, and is similar to a texture-based approach [21], [22] emphasizing the spatial relationships (or inter-relationships) between adjacent voxels. A coherent flow texture corresponds to slight changes in the flow directions between the adjacent flow vectors in a window W, whereas a random flow texture corresponds to large differences in the flow directions between adjacent flow vectors in W. The flow direction changes can be calculated using the dot product operation between the two neighboring flow vectors. Given the normalized velocity vector $v = \{v^x, v^y, v^z\}^T$ indicating the flow direction in a voxel, the relationship between pairs of adjacent vectors can be expressed in a number of ways.

The LPC measure at s is defined as the sum of dot products of these adjacent vector pairs. In this paper, we loosely follow the notations used by Geman and Geman [23] in letting $Z_n = \{1, \ldots, n\}$ represent a regular lattice structure of n voxels (or pixels), and n, the number of voxels in an image. Let $S = \{s_i | i \in Z_n\}$ be a set of voxels, and $V = \{v_i | i \in Z_n\}$ be the corresponding set of normalized flow vectors, and $\mathcal{N} = \{\mathcal{N}_i | i \in Z_n\}$ be a neighborhood system for S. Let W_s be a window at voxel $s \in S$ containing a subset of voxels of S, i.e., $W_s \subset S$. The neighborhood system at s is given by

$$\mathcal{N}_s(c) = \left\{ s_i, s_j \in W_s | 0 < \|s_i - s_j\|^2 \leq c \right\}. \tag{7}$$

Note that c specifies the order of the neighborhood system or the maximum distance $\sqrt{c}$ between two sites s_i and s_j in a window W_s. For example, when $c = 1$, it is a first-order neighborhood system because every voxel inside W_s forms a pair with its nearest neighbor, as shown in Fig. 3(a) for a 3×3 window mask in a slice. A second-order neighborhood system, generated by having $c = 2$, is shown in Fig. 3(b). The LPC measure is defined as

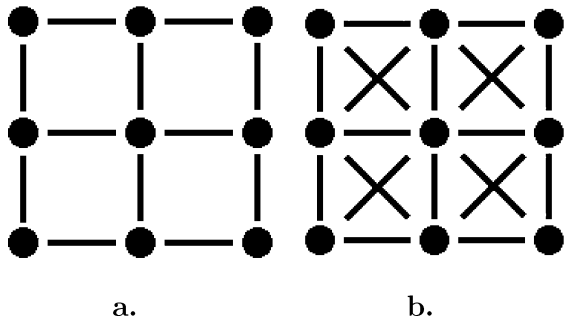

Fig. 3. The neighborhood system $\mathcal{N}_s$. (a) First-order neighborhood system. (b) Second-order neighborhood system.

$$\mathrm{CM}_{\mathrm{lpc}}(c) = \sum_{s_i, s_j \in \mathcal{N}_s(c)} v_i \cdot v_j. \tag{8}$$

In a slice, the number of adjacent vector pairs for $c = 1$ and $c = 2$ are 12 and 20, respectively. $\mathrm{CM}_{\mathrm{lpc}}$ is bounded by the size of the set $\mathcal{N}_s$, i.e., $\mathrm{CM}_{lpc} \in [-\mathcal{N}_s, \mathcal{N}_s]$. Thus, the value range of $\mathrm{CM}_{\mathrm{lpc}}$ is between -12 and 12 when $c = 1$, and -20 and 20 when $c = 2$. The LPC measure is inherently a general measure that can be applied in any dimension. The extension to 3-D is naturally done by applying a $3 \times 3 \times 3$ window cube in an image volume. The size of the neighborhood system, as defined in (7), is then increased. The numbers of adjacent vector pairs $|\mathcal{N}_s|$ for $c = 1$ and $c = 2$ are 54 and 126, respectively. In this paper, a $3 \times 3 \times 3$ window mask (or 3×3 in two dimensions) is used for reasonable localization of the measure and for speed of computation.

In addition to the LPC-based coherence measures introduced in (8), we review two previously defined coherence measures based on: 1) the deviation of vector directions $\mathrm{CM}_{\mathrm{dev}}$ and 2) the ratio of the length of the net flow vector to the total vector length $\mathrm{CM}_{\mathrm{ratio}}$. Given a group of flow vectors V, Rao and Jain [24] suggested projecting the flow vectors onto the mean vector using the dot-product operation, and measured the deviation (or the "spread") of vector directions from the mean vector. This leads to the coherence measure $\mathrm{CM}_{\mathrm{dev}}$ defined as

$$\mathrm{CM}_{\mathrm{dev}} = \frac{\sum_{i \in W} v_i \cdot \bar{v}}{\sum_{i \in W} \|v_i\|} \tag{9}$$

where v_i represents any vector inside a window W and $\bar{v}$ represents the mean vector, which is given by $\bar{v} = (\sum_{i \in W} v_i / N)$, where N is the number of flow vectors inside the window W. It is noted that v_i is a normalized vector, i.e., $\|v_i\| = 1$, because it is intended to measure the directional information alone [24]. Another reason for normalizing the vectors is to avoid any vector with relatively large magnitude dominating the local coherence measurement. Consequently, the coherence measure $\mathrm{CM}_{\mathrm{dev}}$ is bounded by a range between 0 and 1, i.e., $\mathrm{CM}_{\mathrm{dev}} \in [0 \ldots 1]$.

The second approach to measuring flow coherence we consider is that proposed by Summers *et al.* [25]. The coherence measure is defined as

$$\mathrm{CM}_{\mathrm{ratio}} = \frac{\left\|\sum_{i\in W} v_i\right\|}{\sum_{i\in W} \|v_i\|} \tag{10}$$

where v_i represents a normalized vector inside a window W. The coherence measure $\mathrm{CM}_{\mathrm{ratio}}$ represents the ratio of the length of the net flow vectors to the total vector length. Since vectors are normalized, the coherence measure $\mathrm{CM}_{\mathrm{ratio}}$ can be rewritten as

$$\mathrm{CM}_{\mathrm{ratio}} = \frac{\left\|\sum_{i\in W} v_i\right\|}{N} \tag{11}$$

which is bounded between 0 and 1. We introduce the coherence measures in this section as preparation for a comparison of their utility detailed later in this paper.

IV. A Probabilistic Framework for Combining Speed and Flow Coherence Information

To increase segmentation quality, this section introduces a probabilistic framework for combining the *speed* (or flow magnitude) and *flow coherence* information, which have been described in Sections II and III, respectively, for segmentation of brain vessels in PC-MRA datasets.

A. The MAP-MRF Framework

Let $S = \{s_i | i \in Z_n\}$, where $Z_n = \{1, \ldots, n\}$ represent a regular lattice structure with n sites. Let $\mathcal{X} = \{x_i | i \in Z_n\}$ and $\mathcal{Y} = \{y_i | i \in Z_n\}$ be the true image and the observed image, respectively, where x_i can be equal to one of the labels in $L = \{0, 1, 2, \ldots, m-1\}$, y_i represents one of the observed values, e.g., intensity values $\{0, \ldots, I_{\max}\}$ used in Section II, and m is equal to the number of possible classes. Let $\Omega_{\mathcal{X}} = L \times \cdots \times L = L^n$ be the sample space of $\mathcal{X}$, $\mathcal{X} \in \Omega_{\mathcal{X}}$, and $\Omega_{\mathcal{Y}}$ be the observation space, $\mathcal{Y} \in \Omega_{\mathcal{Y}}$.

MAP estimation maximizes the posterior probability $p(\mathcal{X}|\mathcal{Y})$ of the true image $\mathcal{X}$ given the observed image $\mathcal{Y}$. The posterior probability can be estimated according to the Bayes' theorem, $p(\mathcal{X}|\mathcal{Y}) \propto p(\mathcal{X})p(\mathcal{Y}|\mathcal{X})$, where $p(\mathcal{X})$ represents the prior beliefs about the image (prior probability), and $p(\mathcal{Y}|\mathcal{X})$ embodies the knowledge of image formation and noise properties (likelihood function). The MAP decision rule for the optimal solution (final estimated image) $\hat{\mathcal{X}}$ is given by

$$\hat{\mathcal{X}} = \arg\max_{\mathcal{X}\in\Omega_{\mathcal{X}}} p(\mathcal{X})p(\mathcal{Y}|\mathcal{X}). \tag{12}$$

Markov random field (MRF) theory was introduced to the image processing community by Geman and Geman [23] for modeling the local relationships between image voxels so that the optimal solution of the MAP estimation could be obtained in a more robust and efficient manner. We assume that the local relationships between sites in S are described by a neighborhood system $\mathcal{N}$, which is defined as $\mathcal{N} = \{\mathcal{N}_i | i \in Z_n\}$, where $\mathcal{N}_i \subseteq S$ represents a set of sites adjacent to the site s_i. According to the Hammersley-Clifford theorem, $\mathcal{X}$ is a MRF with respect to $\mathcal{N}$ if and only if $p(\mathcal{X})$ is a Gibbs distribution with respect to $\mathcal{N}$. A Gibbs distribution of $\mathcal{X}$ is given by

$$p(\mathcal{X}) = \frac{1}{Z} \times e^{-\frac{U(\mathcal{X})}{T}} \tag{13}$$

where T is a temperature parameter, $U(\mathcal{X})$ is the energy function and Z is a normalizing constant given by $Z = \sum_{\mathcal{X}'\in\Omega_{\mathcal{X}}} e^{-(U(\mathcal{X}')/T)}$, i.e., the normalizing constant is the summation of all the values of possible configurations. Suppose that the likelihood function $p(\mathcal{Y}|\mathcal{X})$ can be expressed in Gibbs distribution form. From (12) and (13), the MAP decision rule becomes

$$\hat{\mathcal{X}} = \arg\max_{\mathcal{X}\in\Omega_{\mathcal{X}}} \left(\frac{1}{Z'} \times e^{-\frac{U(\mathcal{X})+U(\mathcal{Y}|\mathcal{X})}{T}} \right) \tag{14}$$

where Z' is a normalizing constant, and where $U(\mathcal{X})$ and $U(\mathcal{Y}|\mathcal{X})$ denote the prior and likelihood energies, respectively. This in turn leads to a minimization problem, and the MAP decision rule (12) can then be re-expressed as

$$\hat{\mathcal{X}} = \arg\min_{\mathcal{X}\in\Omega_{\mathcal{X}}} \left(\frac{U(\mathcal{X}) + U(\mathcal{Y}|\mathcal{X})}{T} \right). \tag{15}$$

B. Fusing Speed and Flow Coherence Information

A priori knowledge is very important for solving statistical decision problems, like the MAP estimation in (12), because it influences the determination of the posterior probability and in turn affects the decision certainty [26]. We propose a new flow coherence term to represent the prior energy [$U(\mathcal{X})$ in (15)], based on the coherence measure introduced in Section III, such that the information about speed (or flow magnitude) and flow coherence can be incorporated as *a priori* knowledge, and a better quality segmentation can be obtained.

The goal is to partition an image into two separate and distinct regions: 1) the object and 2) the background based on the speed and flow coherence. The process may be summarized as follows. Assume that there exists a flow field in an image, in which flow vectors with different speeds and directions are situated at the center of the sites. Each site variable $x_i \in \mathcal{X}$ will be classified as one of the labels {0, 1}, where $x_i = 1$ if the site belongs to the object having locally coherent flow and relatively high flow (i.e., vessel), and $x_i = 0$ if the site belongs to the background with random and relatively low flow. The MRF $\mathcal{X}$ can be initialized based on the estimated statistical mixture model, as described in Section II, and global thresholding in the speed images. Assume that the flow coherence $\mathcal{O}$ is a constant field, represented at each site s_i by the variable o_i, rather than an MRF because the observed flow field is fixed during the energy minimization process. And further assume that x_i and o_i are located at the same site. Based on the coherence measure, a label o_i is set to 1 if the flow vectors are locally coherent at s_i, and to 0 if the vectors are locally noncoherent. (See Section IV-C for classification of coherent pixels in a LPC map.)

The *a priori* knowledge is derived from the observation that a site s_i is likely to belong to the object class, $x_i = 1$, only if its neighboring object sites and itself are locally coherent, i.e., $x_j = 1$, $o_i = 1$ and $o_j = 1$. The interactions between the sites are described as follows. If $o_i = 0$, then the site belongs

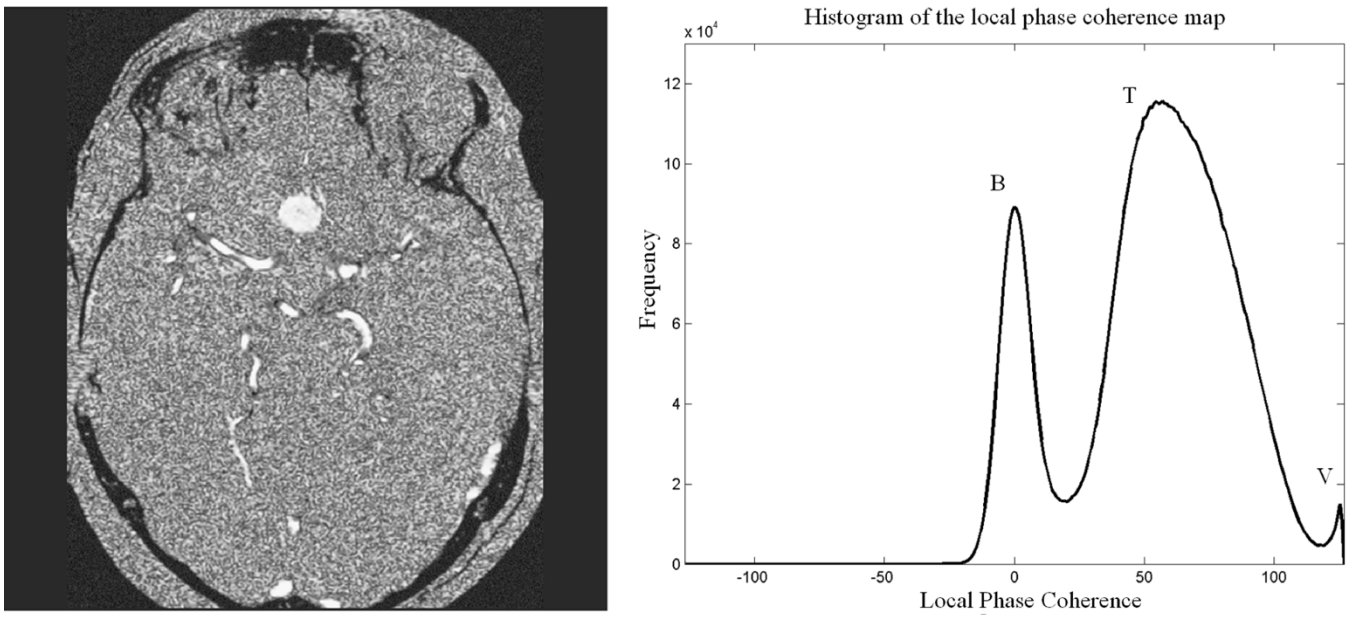

Fig. 4. Local coherence map and its histogram. (a) LPC map. (b) Histogram of the LPC map, which consists of background (B), brain tissue (T) and vessel (V) histograms.

to background, $x_i = 0$. If $o_i = 1$, then the site s_i belongs to the object only if its adjacent sites belong to object $x_j = 1$ and are locally coherent $o_j = 1$; otherwise, $x_i = 0$. Conceptually, these interactions can be similar to boundary or optical flow estimation problems [27], [28]. For example, in boundary estimation, an edge element is commonly estimated in a window, and then neighboring object and edge elements interact in the MRF framework.

The new flow coherence prior energy is defined as

$$U(\mathcal{X},\mathcal{O}) = \sum_{i\in Z_n}\sum_{s_j\in\mathcal{N}_i} \beta_1(1-x_i)x_jo_io_j + \beta_2 x_i(1-x_jo_io_j) \tag{16}$$

where β_1 and β_2 are positive weights, which need not sum to one, and $\mathcal{N}_i$ is the Ising first-order neighborhood system. The parameter β_1 controls the influence of the object sites in the interactions between the adjacent sites, while β_2 governs the weight of the background or noncoherent sites. For instance, setting β_1 to a higher value than β_2 will enhance the interaction between the object-and-coherent sites. As such, from (15), the MAP-MRF decision rule becomes

$$\hat{\mathcal{X}} = \arg\min_{\mathcal{X}\in\Omega_{\mathcal{X}}}\left(\frac{U(\mathcal{X},\mathcal{O}) + U(\mathcal{Y}|\mathcal{X})}{T}\right) \tag{17}$$

where $U(\mathcal{X},\mathcal{O})$ is the new flow coherence prior energy defined in (16) and $U(\mathcal{Y}|\mathcal{X})$ is the likelihood energy.

The derived objective function in (17) can be optimized by the iterated conditional modes (ICM) method [29]. ICM persistently seeks a lower energy configuration and never allows increases in energy, which guarantees a faster convergence rate [5], [29]. ICM assumes that 1) the observed variables $\mathcal{Y} = \{y_i|i \in Z_n\}$ are conditionally independent, and 2) the state of a site s_i depends only on the states of its adjacent sites $\mathcal{N}_i$ (Markovian property). These two assumptions allow the minimization of its local energy terms

$$\left[\sum_{s_j\in\mathcal{N}_i}\beta_1(1-x_i)x_jo_io_j + \beta_2x_i(1-x_jo_io_j)\right] + U(y_i|x_i) \tag{18}$$

at site s_i in each iteration step such that the overall energy terms $U(\mathcal{X},\mathcal{O})+U(\mathcal{Y}|\mathcal{X})$ in (17) can be minimized. It should be noted that we fixed the temperature T throughout the entire searching process, e.g., $T = 1$.

C. Application to PC-MRA Images

In this section, we apply the MAP-MRF approach to the segmentation of PC-MRA images. A typical LPC map and its histogram are shown and plotted in Fig. 4(a) and (b), respectively. The second-order LPC , $\mathrm{CM}_{\mathrm{lpc}}(c = 2)$, is used. Fig. 4(b) shows that the histogram is right-shifted and skewed.

In fact, the LPC histogram can be described by three classes: background with low LPC, brain tissue with slightly higher LPC, and vessel with extremely high LPC, as illustrated in Fig. 4(b). The vessel (V) and brain tissue (T) histograms overlap because of the nonstationary, but slightly coherent motion of the nonvessel brain tissue, and systematic imaging artefacts [30]. As in Section II, where we modeled the background and vascular signals in speed images, we model the background and brain tissue regions in LPC maps with two separate Gaussian distributions. It is worth noting that theoretical modeling of the LPC histogram is extremely difficult. This is because of the high correlation between the velocity random variables, and normalization and dot product operations of the correlated variables when the coherence measure is calculated. We again use the EM algorithm to fit the LPC histogram by a mixture

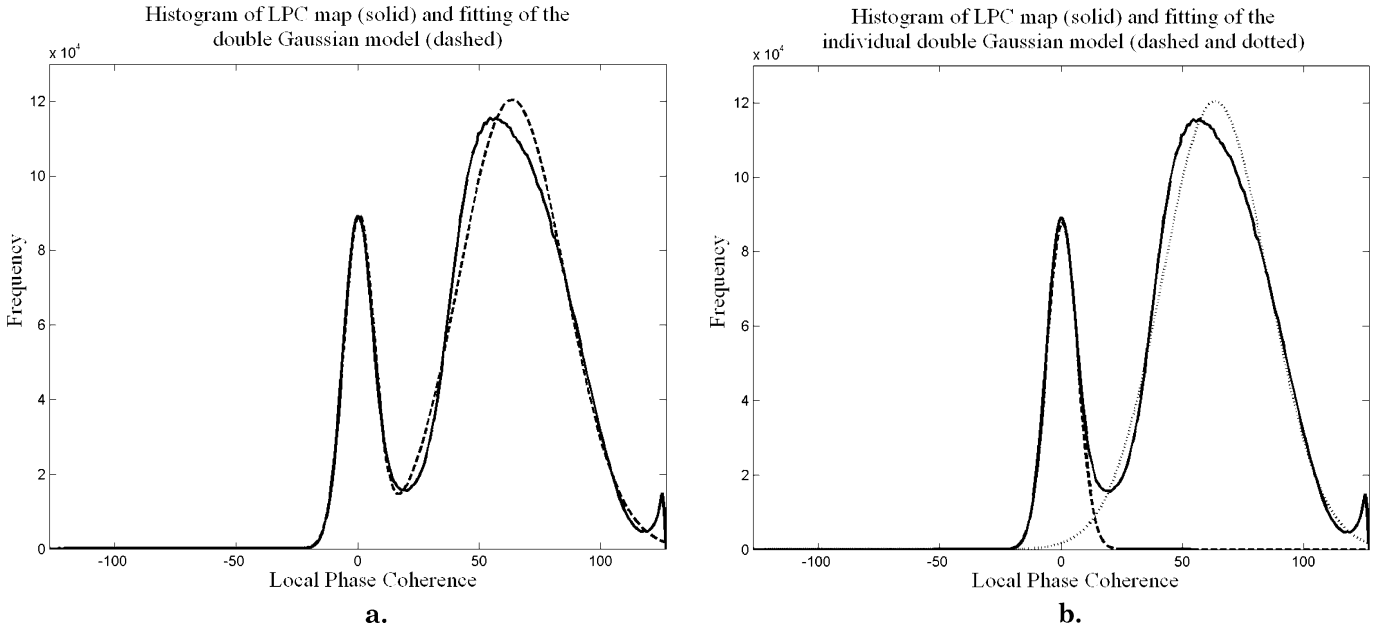

Fig. 5. LPC histogram and the double Gaussian model, with a second-order neighborhood system. (a) Histogram of LPC map and fitting of the double Gaussian model. (b) Individual histograms of the Gaussian distributions.

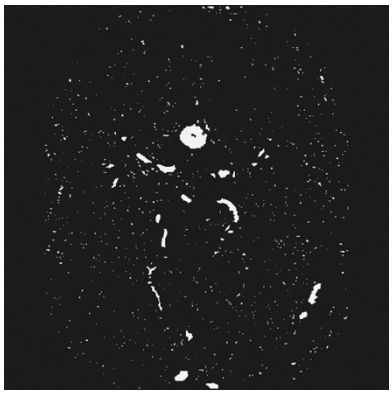

Fig. 6. Coherent voxels.

of the two Gaussian distributions. Fig. 5(a) shows the fitting of the double Gaussian model (dashed line). The individual histograms of the Gaussian distributions are shown in Fig. 5(b).

We define the mean and standard deviation of the brain tissue distribution as μ_T and σ_T, respectively, and use $\mu_T + \alpha \cdot \sigma_T$ as the nonvessel threshold (we set α equal to 2 in this paper), which is a variant of the background thresholding approach [31], [32]. A voxel with LPC above the nonvessel threshold is labeled as a coherent voxel. Otherwise, it is labeled as a noncoherent voxel. As shown in Fig. 6, the coherent voxels form a number of vessel "clusters," though there are some randomly distributed voxels due to random coherent noise, small coherent motion of the nonvessel tissue during scanning and ghosting artefacts. These "outliers" can be ignored if they are far away and disconnected from the vasculature, and their intensity values in a speed image are low.

The proposed segmentation algorithm, based on the MAP-MRF model and using the flow coherence prior energy, is summarized as follows.

1) Use mixture model and global thresholding to obtain a) a segmented PC-MRA speed image $\mathcal{X}$, in which $x_i = 1$ and $x_i = 0$ represent object and background sites, respectively; and b) the local likelihood energy $U(y_i|x_i)$. (see Section II)

   For the background sites, $x_i = 0$,
   if the MGU mixture model is used, then $U(y_i|x_i = 0) = -\log((w_M f_M(y_i) + w_G f_G(y_i))/(w_M + w_G))$ or
   if the MU mixture model is used, then $U(y_i|x_i = 0) = -\log f_M(y_i)$.

   For the object sites, $x_i = 1$,

$$U(y_i|x_i = 1) = -\log f_U(y_i).$$

2) Compute the coherence measure $\mathrm{CM}_{\mathrm{lpc}}(c = 2)$ at each site. (see Section III)

3) Segment the image $\mathcal{O}$ based on $\mathrm{CM}_{\mathrm{lpc}}(c = 2)$, where $o_i = 1$ and $o_i = 0$ represent coherent and noncoherent sites, respectively, and x_i and o_i are located at the same site position. (see Section IV-C)

4) Iterate for $k = 1, \ldots, MaxItn$: (see Section IV-B)

   Iterate for $i = 1, \ldots, n$:

$$x_i^k = \arg \min_{x_i^k \in \{0,1\}} \left(U\left(x_i^k | o_i, x_j^{k-1}, o_j\right) + U\left(y_i | x_i^k\right) \right)$$

   where

$$U\left(x_i^k | o_i, x_j^{k-1}, o_j\right) = \sum_{s_j \in \mathcal{N}_i} \beta_1 \left(1 - x_i^k\right) x_j^{k-1} o_i o_j + \beta_2 x_i^k \left(1 - x_j^{k-1} o_i o_j\right)$$

   Terminate if $\mathcal{X}^{k-1} = \mathcal{X}^k$ or $k = MaxItn$.

5) Final estimate $\hat{\mathcal{X}} = \mathcal{X}^k$.

(Note: $MaxItn$ = Maximum number of iterations. n = Total number of sites.) The final estimate $\hat{\mathcal{X}}$ becomes the output of the segmentation method.

V. Experiments and Results

To assess the performance of the proposed segmentation method, our approach has been applied to clinical, synthetic and flow phantom datasets. These studies were conducted in collaboration with the University Hospital of Zurich, Switzerland, who performed the data acquisition. All the datasets were acquired using a Philips 3T ACS Gyroscan MR scanner. The segmentation process was implemented in Visual C++ 6.0 with the use of MATLAB 6.0 Release 12 as an interface, and was run on a 1.8-GHz PC in the MS Windows NT environment with 512–MB RAM.

A. Model Selection Mechanism

For validation, both the MGU and MU models were fitted to the observed intensity histograms of 12 PC-MRA speed image volumes. We have noted that, when the MU mixture distribution approximates the observed intensity histogram well, the Gaussian component of the MGU mixture model has a relatively large variance and small weight w_G. This flattened Gaussian component may lead to an excessively high estimate for the image threshold I_{MGU}, and a suboptimal segmentation. As shown in Table I, this occurred in 7 out of the 12 test cases (Volumes: 1,2,4,5,6,10,11) (One example is shown in Fig. 1).

The mixture model selection procedure described in Section II was used in each case. For comparison, a consultant radiologist was asked to choose between the MU and MGU models on the basis of which of the above detailed segmentations more closely matched his evaluation of the speed images. For each case, a PC-MRA speed volume and its two globally segmented volumes were presented (one based on the MU model and the other on the MGU model). Table I gives the values of J_1 and J_2, together with the selection of mixture model made by the automated KLD-based method and by the expert reader for each of the 12 clinical PC-MRA datasets. From the table, the results show that models selected by the KLD-based method and models selected manually by a radiologist are well matched. On average, the computational time was around 2 s for the relatively large volume matrix size of $512 \times 512 \times 64$ voxels.

TABLE I
Image Thresholds I_{MGU} and I_{MU} Estimated by the MGU and MU Mixture Models, Respectively. (Maximum Intensity Value of the Observed Histograms Is 2048 for All Vols.) It Also Gives the Values of J_1 and J_2, and the Selected Mixture Models (by the KLD-Based Method and Manual Selection) for the 12 PC-MRA Speed Image Volumes. It Shows That Models Selected by the KLD-Based Method and Models Selected Manually by a Radiologist Are Well Matched

	Vol. 1	Vol. 2	Vol. 3
I_{MGU}	475	351	284
I_{MU}	248	104	245
J_1	0.04427	0.4392	0.1710
J_2	0.0006870	0.001253	0.9810
Selected mixture models			
KLD-based method	MU	MU	MGU
Manual selection	MU	MU	MGU
	Vol. 4	Vol. 5	Vol. 6
I_{MGU}	307	299	442
I_{MU}	96	89	146
J_1	0.4137	0.4568	0.2824
J_2	0.002012	0.002532	0.0008525
Selected mixture models			
KLD-based method	MU	MU	MU
Manual selection	MU	MU	MU
	Vol. 7	Vol. 8	Vol. 9
I_{MGU}	180	241	180
I_{MU}	147	201	149
J_1	0.1567	0.1131	0.1382
J_2	0.4285	0.3167	0.3950
Selected mixture models			
KLD-based method	MGU	MGU	MGU
Manual selection	MGU	MGU	MGU
	Vol. 10	Vol. 11	Vol. 12
I_{MGU}	500	394	170
I_{MU}	195	122	153
J_1	0.1848	0.2702	0.01764
J_2	0.001334	0.0006468	0.06064
Selected mixture models			
KLD-based method	MU	MU	MGU
Manual selection	MU	MU	MGU

B. Synthetic Image Volumes

In this study, the synthetic image volumes consist of two flow patterns: 1) vertical straight tubes and 2) circular tubes with diameters of 8 and 4 voxels, as shown in Fig. 7(a) and (b), respectively (middle slices of the volumes). The typical vessel dimensions encountered *in vivo* are on average 8 voxels for large vessels down to 4 (or fewer) voxels for the smaller vessels. The simulated parameters were, therefore, chosen to mimic the clinical case. The image volume sizes were $256 \times 256 \times (8+2)$ and $256 \times 256 \times (4+2)$, respectively (The extra two image slices are the top and bottom background slices). The white strips in Fig. 7(a) and (b) represent the positions and regions of the simulated flow, while the black strips represent the background regions. In Fig. 7(a), the simulated "flow" runs from top to bottom direction, while in Fig. 7(b), it is in the clockwise direction.

For the purpose of image synthesis, we corrupt each velocity component with Gaussian noise having zero mean and the same standard deviation σ [33]. In Fig. 7(a), the flow vector inside the tubes is given by $v_x = n_x$, $v_y = -A + n_y$, and $v_z = n_z$, where A represents the true flow magnitude, the y axis is parallel to the tube direction, and the terms n_x, n_y and n_z are the zero-mean Gaussian noise components with the same standard deviation σ. The flow vector in the background is given by the same set of equations, except that A is set to zero. SNR is then given by $\mathrm{SNR} = A/\sigma$. Similarly, the tube flow vector in Fig. 7(b) is given by $v_x = A \times sin\theta + n_x$, $v_y = -A \times \cos\theta + n_y$, and $v_z = n_z$, where $\theta \in [0 \ldots 2\pi]$. As with clinical practice, voxels with high flow rates are assigned intensity values higher than those assigned to the voxels with low flow rates. The magnitude (or the speed) of the flow at each voxel is given by $m = \sqrt{v_x^2 + v_y^2 + v_z^2}$. In our datasets, the SNR of typical

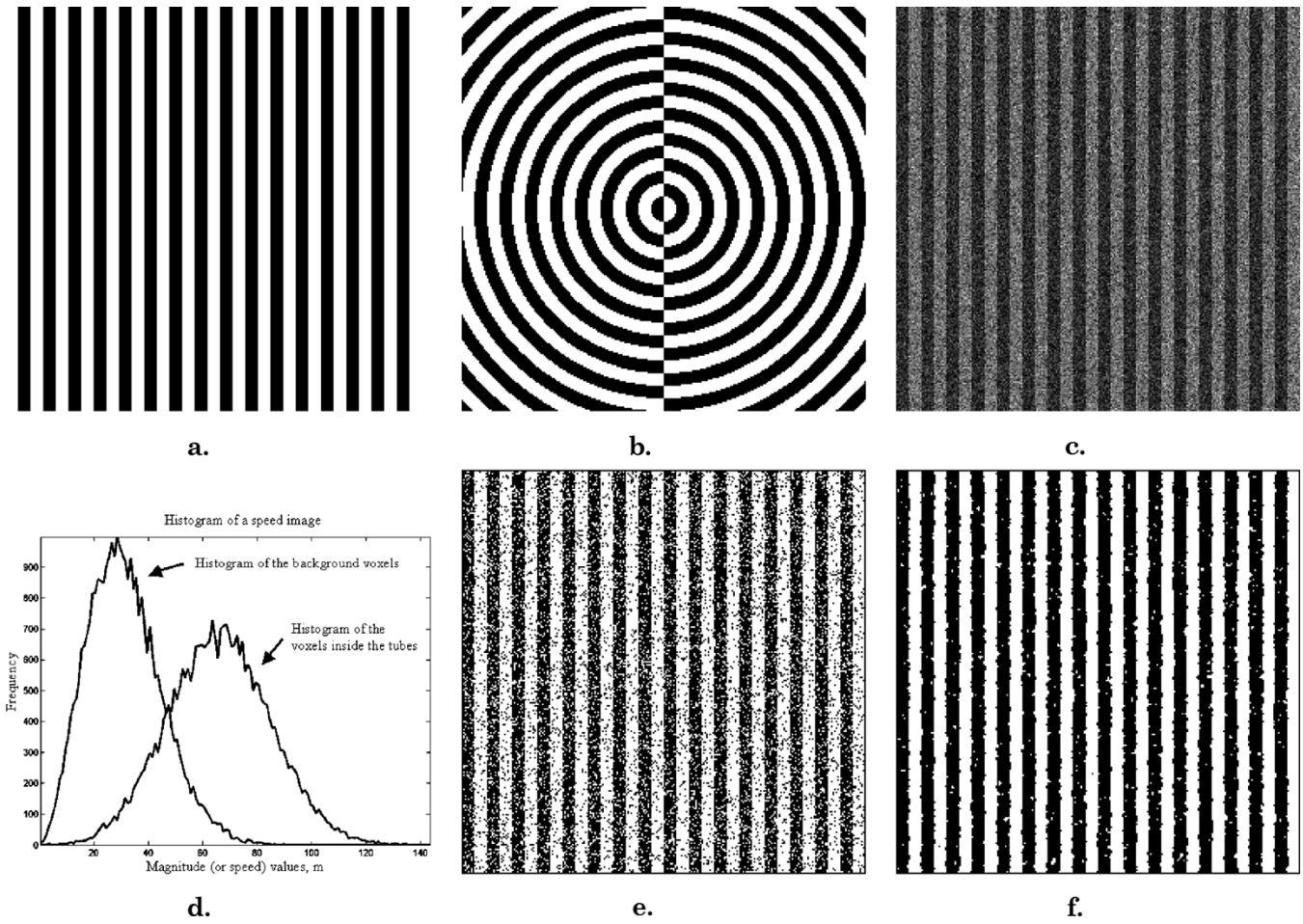

Fig. 7. True patterns of the synthetic images (tubes are 8 pixel width). (a) Vertical straight tubes. (b) Circular tubes. (c) Speed image of the synthetic flow patterns ($\mathrm{SNR} = 3$). (d) Speed image histogram of (c). (e) Segmented image using speed information alone. $\mathrm{Segmentation\ error} = 13.75\% \pm 0.0320\%$. (f) Segmented image using $\mathrm{CM}_{\mathrm{lpc}}(c = 2)$. $\mathrm{Segmentation\ error} = 0.95\% \pm 0.0140\%$.

major arteries in the brain can range from 4 (near the boundary) to 40 or more (vessel center), which mainly depends on the flow magnitude. For veins, the SNR can range from 3 to 20. For aneurysms, the SNR can range from 3 (sac) to 20 (near the aneurysmal wall).

Fig. 7(c) shows the speed images of the synthetic flow patterns ($\mathrm{SNR} = 3$). The histogram corresponding to the simulated image is plotted in Fig. 7(d). The background distributions overlap heavily with those of the tubes because of the low SNR ($\mathrm{SNR} = 3$). Segmentation was then performed using the MAP method on the histograms of vessel and background voxels in the speed images to choose the intersections of the histograms as the threshold. Fig. 7(e) shows that, when the SNR is low, segmentation result based on the speed information alone is not very encouraging. Coherence maps of $\mathrm{CM}_{\mathrm{lpc}}(c = 2)$ (8) were then calculated on a voxel-by-voxel basis. We generated histograms of the background and tube regions from the corresponding coherence maps. The background and tube histograms were then used for thresholding the coherence maps using the MAP classification method. An example of the thresholded image for $\mathrm{CM}_{\mathrm{lpc}}(c = 2)$ is shown in Fig. 7(f). It is observed that the thresholded image matches the true flow patterns [Fig. 7(a)] better than the segmented image obtained using speed information alone [Fig. 7(e)].

TABLE II
SEGMENTATION ERRORS BASED ON $\mathrm{CM}_{\mathrm{lpc}}(c = 2)$, $\mathrm{CM}_{\mathrm{lpc}}(c = 1)$, $\mathrm{CM}_{\mathrm{ratio}}$, $\mathrm{CM}_{\mathrm{dev}}$ AND SPEED INFORMATION ALONE. (TUBE SIZE = 8 PIXELS, SNR = 3.)

Coherence Measures	(Tube Type) Vertical	(Tube Type) Circular
$CM_{lpc}(c = 2)$	$0.9450\% \pm 0.0140\%$	$2.0396\% \pm 0.0038\%$
$CM_{lpc}(c = 1)$	$1.4716\% \pm 0.0130\%$	$2.7651\% \pm 0.0173\%$
CM_{ratio}	$2.2501\% \pm 0.0361\%$	$3.2875\% \pm 0.0134\%$
CM_{dev}	$2.2448\% \pm 0.0387\%$	$3.2815\% \pm 0.0136\%$
Speed info. alone	$13.7530\% \pm 0.0320\%$	$13.6632\% \pm 0.0598\%$

Given that the true pattern is known, the segmentation error can be accurately calculated by counting the number of misclassified pixels, which is given by

$$\mathrm{Error} = \frac{\mathrm{Number\ of\ misclassified\ pixels}}{\mathrm{Total\ number\ of\ pixels\ in\ the\ image}} \times 100\%. \tag{19}$$

Tables II and III list the segmentation errors based on $\mathrm{CM}_{\mathrm{lpc}}$, $\mathrm{CM}_{\mathrm{ratio}}$ (11), $\mathrm{CM}_{\mathrm{dev}}$ (9) and speed information alone, and also provide relative performance of $\mathrm{CM}_{\mathrm{lpc}}$ when $c = 1$ and $c = 2$.

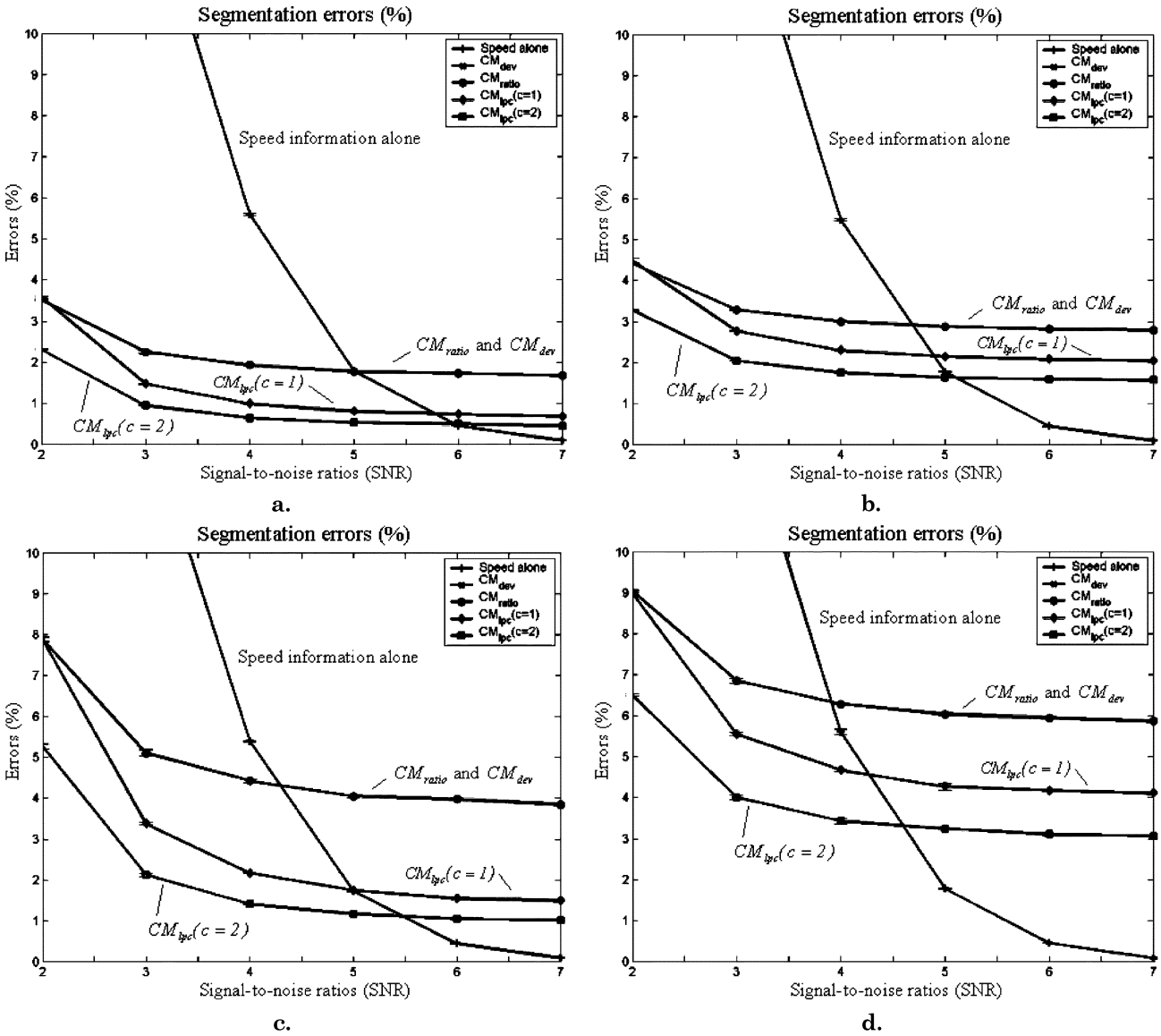

Fig. 8. Errors of segmentation using three-dimensional (3-D) flow coherence information from the synthetic images (vertical and circular tubes). (a) Vertical straight tubes (8-voxel width). (b) Circular tubes (8-voxel width). (c) Vertical straight tubes (4-voxel width). (d) Circular tubes (4-voxel width).

TABLE III
SEGMENTATION ERRORS BASED ON $\mathrm{CM}_{\mathrm{lpc}}(c=2)$, $\mathrm{CM}_{\mathrm{lpc}}(c=1)$, $\mathrm{CM}_{\mathrm{ratio}}$, AND $\mathrm{CM}_{\mathrm{dev}}$. (TUBE SIZE = 4 PIXELS, SNR = 3.)

Coherence Measures	(Tube Type) Vertical	(Tube Type) Circular
$CM_{lpc}(c=2)$	$2.1188\% \pm 0.0356\%$	$4.0043\% \pm 0.0509\%$
$CM_{lpc}(c=1)$	$3.3724\% \pm 0.0288\%$	$5.5450\% \pm 0.0357\%$
CM_{ratio}	$5.0975\% \pm 0.0732\%$	$6.8573\% \pm 0.0532\%$
CM_{dev}	$5.1136\% \pm 0.0738\%$	$6.8589\% \pm 0.0559\%$
Speed info. alone	$13.3015\% \pm 0.0343\%$	$13.7798\% \pm 0.0581\%$

The simulations were repeated for 12 different noise contributions at each of the six SNR levels between 2 and 7. The tables reveal that, when $\mathrm{SNR} = 3$, $\mathrm{CM}_{\mathrm{lpc}}$ consistently gives a smaller segmentation error than $\mathrm{CM}_{\mathrm{ratio}}$ and $\mathrm{CM}_{\mathrm{dev}}$. Compared to the segmentation errors using speed information alone, it is clear that segmentation using flow coherence information gives higher segmentation accuracy when the SNR is low.

The segmentation errors of the four different coherence measures are plotted in Fig. 8 across a range of different SNRs for the synthetic images. It is interesting to see that the segmentation errors change significantly as the SNR increases (from $\mathrm{SNR} = 2$ to $\mathrm{SNR} = 7$). Most notably, there is a performance transition *from* [Fig. 8(a)] low SNR (i.e., less than 4), where the quality of segmentation using flow coherence information is better than that using speed information alone; *to* [Fig. 8(b)] high SNR (i.e., larger than 4), where segmentation using speed information alone is better than that using flow coherence information.

The two major behaviors seen in segmenting these images can be understood in the following way. First, speed histograms overlap heavily when the SNR is low, making the MAP segmentation based on speed information problematic and increasing the segmentation error. In this situation, the spatial correlation of flow vectors provides more robust information than the speed information for segmentation with a noisy background. Secondly, speed histograms become well separated when the SNR is high. As such, the segmentation error using speed information

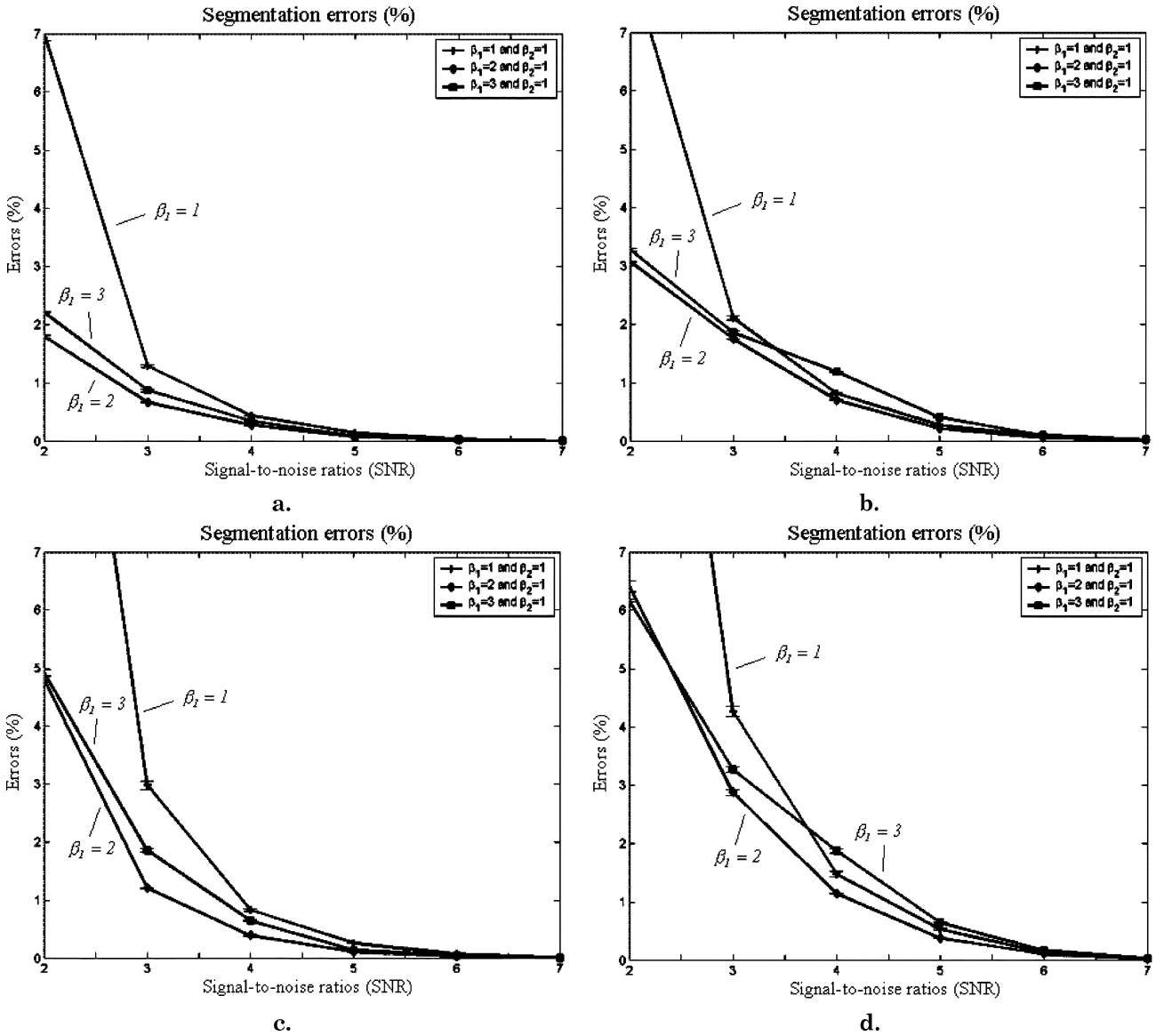

Fig. 9. Segmentation errors on the 3-D synthetic images (vertical and circular tubes). Different values of $\beta_1 = 1, 2, 3$ and fixed value of $\beta_2 = 1$. (a) Vertical straight tubes (8 voxel width). (b) Circular tubes (8 voxel width). (c) Vertical straight tubes (4 voxel width). (d) Circular tubes (4 voxel width).

is greatly reduced. The reduction in segmentation error using flow coherence information, however, is limited by inevitable errors due to the tube boundaries (flow discontinuities) and the inherent random coherence patterns in the background.

Fig. 8 also shows that, among the four different coherence measures, $\mathrm{CM}_{\mathrm{lpc}}(c = 2)$ and $\mathrm{CM}_{\mathrm{lpc}}(c = 1)$ give better overall segmentation results than $\mathrm{CM}_{\mathrm{dev}}$ and $\mathrm{CM}_{\mathrm{ratio}}$ in the two synthetic image volumes with the tube diameter set to 8 and 4 voxels. Moreover, $\mathrm{CM}_{\mathrm{lpc}}(c = 2)$ gives a smaller segmentation error than $\mathrm{CM}_{\mathrm{lpc}}(c = 1)$.

Although only tube widths of 8 and 4 were tested, it can be expected that the segmentation error decreases as the tube width increases for both straight and circular tubes. For example, the segmentation errors drop when the width increases from 4 voxels [see Fig. 8(c) and (d)] to 8 voxels [see Fig. 8(a) and (b)]. The errors of the wider tubes are smaller than those of the narrower tubes. The reason is described as follows. As the width increases, the curvature on the tube surface decreases. For estimating local coherence on the tube surface, the decrease in curvature can lead to an increase in the number of flow vectors within a window W_s (7). Therefore, more evidence is included to give a more reliable decision on the local coherence. Similarly, because of the decrease in the curvature of surfaces, it is observed that the segmentation errors of the vertical tubes [see Fig.8 (a) and (c)] are smaller than those of the circular tubes [see Fig. 8(b) and (d)].

Based on the proposed MAP-MRF method using both speed and flow coherence information, we further segmented the four synthetic 3-D image volumes using different values of β_1 and a fixed value of β_2 (β_2 was set to 1 throughout this paper), and compared the differences in segmentation when β_1 was varied from 1 to 3. The segmentation performance was measured based on the ratio of the number of misclassified pixels to the total number of voxels, which is defined in (19). From Fig. 9, it is observed that the segmentation performance is sensitive to the value of β_1 when the SNR is low. This is because, in the low SNR regions, the segmentation performance mainly depends on the interactions between adjacent sites based on the flow coherence information, and the interaction is enhanced by setting a higher value of β_1.

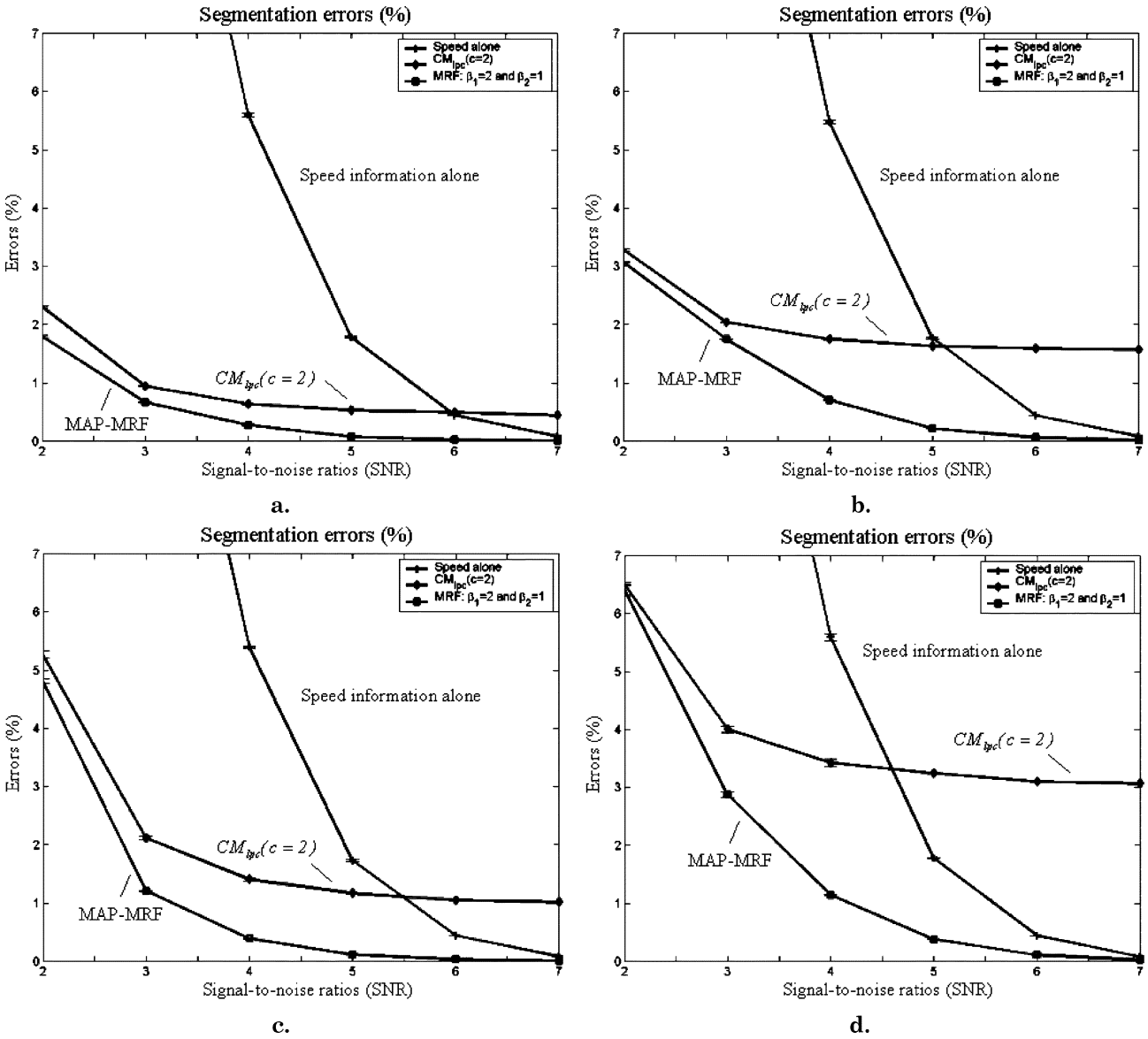

Fig. 10. Comparison on the results based on 1) segmentation using speed information alone, 2) segmentation using flow coherence information alone, and 3) segmentation using both speed and flow coherence information. All segmentations were done on the 3-D synthetic images (vertical and circular tubes). $\beta_1 = 2$ and $\beta_2 = 1$. (a) Vertical straight tubes (8 voxel width). (b) Circular tubes (8 voxel width). (c) Vertical straight tubes (4 voxel width). (d) Circular tubes (4 voxel width).

Fig. 9 also shows that when $\beta_1 = 2$, segmentation errors are smaller than the other two values, $\beta_1 = 1$ and 3, over the whole range of SNRs (from 2 to 7). As such, we set $\beta_1 = 2$ in this implementation. From the figure, it can be predicted that the segmentation errors are small when the SNR is large, and also the difference between $\beta_1 = 1$, 2 and 3 becomes very small.

Fig. 10 shows the results of the three different segmentation methods, based on 1) speed information alone, 2) flow coherence information alone using the second-order local flow coherence measure $\mathrm{CM}_{\mathrm{lpc}}(c = 2)$, and 3) the MAP-MRF model using both speed and flow coherence information. As shown in Fig. 10, the combination of speed and flow coherence information in the MAP-MRF model substantially reduced the overall segmentation errors at all SNR levels tested.

C. Flow Phantom and Measurement of Error

A geometrically accurate straight tube flow phantom was made using MR compatible materials (silicone elastomer, Sylgard 184, Dow Corning Corp, Midland, MI). The phantom was constructed using a lost metal technique based on a numerically controlled, milled mould [34]. The phantom provides accurately defined lumen dimensions, which are 8 mm in diameter running the length of the silicon block (block dimensions: $240 \times 120 \times 25\ \mathrm{mm}^3$). The phantom was filled with a water glycerol mixture having a viscosity comparable to that of human blood flowing at a constant rate of $300\ \mathrm{mm/s}$. The phantom was scanned using the PC-MRA protocol on a 1.5T MR scanner (Signa, GE Healthcare, Milaukee WI) at the Department of Neuroscience, King's College London, London, U.K. The image size was $256 \times 256 \times 40$ voxels and dimensions were $0.625 \times 0.625 \times 1.3\ \mathrm{mm}^3$. The scan details were as follows: axial scan, $\mathrm{TE/TR} = 7.3/20$ ms, flip angle 18°, 1 signal average, FOV: $22 \times 16\ \mathrm{cm}^2$, VENCS: $400\ \mathrm{mms}^{-1}$ and acquisition matrix: 256×160 pixels.

Fig. 11 shows a MIP of the straight tube. The image has been cropped for the purpose of illustration. The left- and

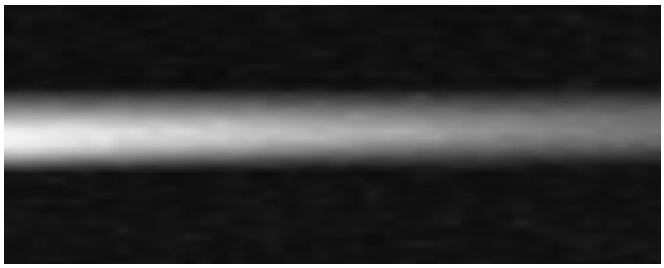

Fig. 11. Maximum intensity projection of the straight tube phantom. The left– and right-hand sides are the inflow and outflow regions, respectively.

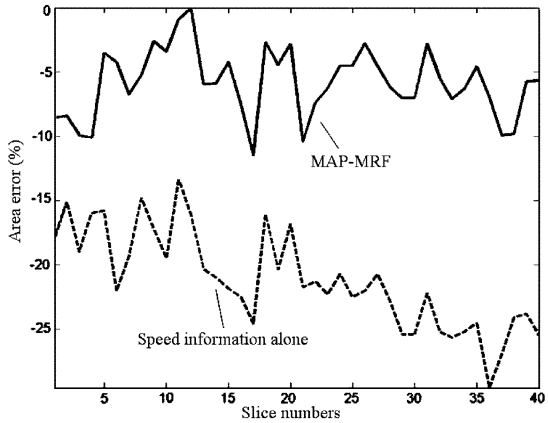

Fig. 12. This figure shows that the errors of area estimation (underestimation) are $-5.83\% \pm 2.64\%$ and $-21.19\% \pm 3.76\%$ for the MAP-MRF-based approach and method using speed information alone, respectively. The difference between two methods is 15.36%.

right-hand sides are the inflow and outflow regions, respectively. Although the speed inside the tube remained constant during the experiments, the SNR decreases from the inflow region to the outflow region due to progressive saturation of the fluid signal. Also, it is recognized that imperfections in velocity encoding due to nonlinearities in the gradient systems can cause a position-dependent deviation in the velocity images [30]. These two factors may influence the behavior of the surface extraction method but were not taken into consideration in the experiments below.

We define the measurement error in a slice as the percentage difference between the estimated area and the true area of the straight tube

$$\text{Error} = \frac{A_{\text{estimated}} - A_{\text{true}}}{A_{\text{true}}} \times 100\% \qquad (20)$$

where $A_{\text{estimated}}$ and A_{true} represent the estimated and true areas, respectively. For validation, we invited a consultant radiologist to segment each slice manually. The manual segmentations were used for estimating the true area by counting the number of pixels inside the tube and multiplying the voxel size $(0.625^2\ \text{mm}^2)$ in a slice. The estimated area $A_{\text{estimated}}$ is equal to the number of vessel voxels multiplied by the voxel size. As such, the error is negative when $A_{\text{estimated}}$ underestimates the true area.

Fig. 12 shows the results of applying segmentation based on speed information alone, and based on the MAP-MRF method described in Section IV-C to the straight tube phantom using the

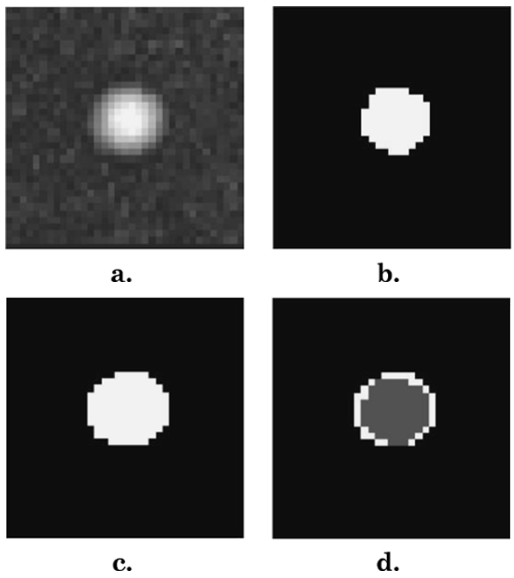

Fig. 13. Segmentation results and comparison. (a) Original speed image. (b) Segmented image using speed information alone. (c) Segmented image using speed and flow coherence information. (d) The differences between (b) and (c) are white in color, and the overlapping vessel region is grey in color.

area error defined in (20) as the measure of comparison. This figure shows that the MAP-MRF-based approach using both speed and flow coherence information gives higher segmentation accuracy (on average, $-5.83\% \pm 2.64\%$ of the true area, underestimated) than the segmentation method using speed information alone (on average, $-21.19\% \pm 3.76\%$ of the true area, underestimated). The underestimation can be caused by the fluid viscosity. The frictional force can slow down the flow near the wall [35]. As such, the intensity is relatively low at the boundary in the angiograms. This can make segmentation inaccurate near the tube wall.

Fig. 13(a) shows an example speed image of the flow phantom data, in which the cross-section of the phantom is located at the center. Fig. 13(b) and (c) shows the segmentation results of using speed information alone and the MAP-MRF method. The differences between these two images are shown as white, and the overlapping vessel region as grey in Fig. 13(d), which reveals the advantage of incorporating flow coherence information for segmenting the low SNR regions near the boundary of the tube.

If we assume that the cross-sectional areas are in circular shape, then the underestimations of areas, 5.83% for MAP-MRF and 21.19% for speed information only based segmentations, can be seen against the pixel resolution of the images. For this phantom, the typical tube diameters are around 11 and 12 pixels, and so a single pixel represents between 5% and 6% of the vessel lumen. Thus, the results of the MAP-MRF method and segmentation using speed information alone correspond to underestimations representing less than 1 and approximately 4 pixels underestimation, respectively. Because the underestimation is not a focal effect but is smoothly dependent on position in the phantom, the erroneous pixel excluded from the cross-section will not result in specific stenosis, but rather irregularity of the segmented surface. The impact of this error, however, is likely to increase as the vessel size is reduced.

D. Clinical Studies

We have applied our approach to 12 clinical datasets. Some representative segmentation results are shown in Fig. 14. For the sake of comparison, the clinical PC-MRA images [as shown in Fig. 14(a)] were first processed using speed information alone [see Fig. 14(b)], as described in Section II. The overall segmentations are good except for the regions of low or complex flow indicated by the arrows. The resulting loss in contrast makes the vessel voxels hard to distinguish from the background voxels. The results of applying the MAP-MRF segmentation algorithm combining speed and flow coherence information are shown in Fig. 14(c). It can be seen that there are improvements in segmentation, especially within aneurysms, and other low flow regions, e.g., veins. In Fig. 14(d), the differences between Fig. 14(b) and (c) are highlighted in white, while the vessel regions identified in both 14(b) and 14(c) are depicted in grey. To visualise the shape of reconstructed vasculatures, MIPs of two PC-MRA volumes are shown in Fig. 15(a) and (d). The three dimensional surfaces of the segmented results based on speed information alone are shown in Fig. 15(b) and (e). Fig. 15(c) and (f) shows the improved surfaces based on the segmentation method using speed and flow coherence information. Aneurysms and veins are indicated in these figures by solid and dashed arrows, respectively.

We note that, in some cases, there remain a few false-negative voxels (two or three voxels) in the middle of the indicated regions. We have found two main reasons for this. First, the flow rate was extremely low in the middle, which may lead to serious corruption of the velocity field by noise. Second, a circular (or deformed circular) flow pattern in the aneurysm will give rise to an associated singularity in the flow field. These factors can adversely affect the LPC measure. The average computation time, on average for all cases, is about 20 min for the relatively large volume matrix size of $512 \times 512 \times 64$ pixels.

VI. Summary and Discussion

In this paper, we have introduced the use of statistical mixture models for modeling the background and vascular signals in clinical PC-MRA images. One of the main contributions of this paper is that we have proposed a way of selecting between the MGU and MU mixture models based on the KLD measure. Experiments carried out on 12 clinical images illustrated the applicability of the MGU and MU mixture models, and showed that the KLD measure can help in selecting the appropriate threshold for the segmentation task.

Although the mixture model works satisfactorily in classifying the background and vessel voxels, for relatively low flow rate and low SNR vessel regions, e.g., aneurysms and veins, we find that it is hard to distinguish vessel voxels from the background voxels because of their low intensity value. Rather than relying on the speed information alone, the available but unused velocity information is used to overcome this problem. We have formally introduced a flow coherence term into the image segmentation process, and presented a local coherence measure, namely the LPC measure, which effectively describes the spatial correlations of the neighboring flow vectors. We have carried out experiments on synthetic images to evaluate and compare the performance of the LPC measure and two other related coherence measures that have appeared in the literature. The experimental results show that 1) when the SNR is low, segmentation using the flow coherence measure is more accurate than that achieved using just the speed information, 2) the LPC measure outperforms the two other related coherence measures, and 3) the second-order LPC measure $(\mathrm{c} = 2)$ performs better than the first-order LPC measure $(\mathrm{c} = 1)$ because it gives more evidence of flow vector correlations. On the other hand, when the SNR is high, segmentation simply using a threshold based on the speed information outperforms that attained when only the coherence measure information is incorporated.

In PC-MRA datasets, different vessel dimensions and contained flow velocities create a range of SNRs for the vessels. Those vessels with high SNRs can be readily segmented based on the speed image alone. The use of the velocity information alone through a measure of LPC is less error prone at low SNRs, but is subject to errors in the presence of background boundaries or flow singularities. The combination of these methodologies in an automated framework is a promising step forward. In this paper, we have presented a MAP-MRF framework for combining speed and flow coherence information for segmentation. Experiments on synthetic images show that the new method reduces segmentation errors across SNRs ranging from $\mathrm{SNR} = 2$ to 7. Furthermore, experiments on a flow phantom (straight tube) show that the MAP-MRF method is more accurate than the method using speed information alone. Finally, the performance of the MAP-MRF method was evaluated on 12 clinical datasets. Testing on the datasets showed that the combined approach performs better than the approach using speed information alone in segmenting vasculature and low flow regions, e.g., aneurysms and veins.

The MU and MGU models were adapted to fit the physics and mathematics underlying the generation of PC-MRA images. Future work will include detection of flow singularities which may indicate the presence of vorticity (to be expected in large saccular aneurysms), perhaps by using knowledge of flow topology.

When the level of SNR goes down to about 2, the velocity field obtained from the PC-MRA images can be seriously corrupted by noise. It can be described as the "velocity estimates corrupted by noise" domain, which is likely to be found in the background regions. For a better estimation of LPC, other forms of preprocessing or further knowledge of flow topology [36] (e.g., lack of field divergence) can be incorporated. Using those preprocessing techniques one should also consider the fact that there may be systematic errors in the velocity field estimates due to misalignment of spatial encoding for moving spins, or nonsteady velocities (always present to some degree due to cardiac pulsation).

We will also investigate the improvements on the inclusion of flow coherence information in the segmentation method, especially on the possibilities of eliminating the necessity for thresholding the LPC map. While flow coherence is relevant to the angiographic application to hand, other sources of secondary information could be used as in multispectral analysis of different MR images. Closely akin to the present work is high resolution MR venography where the low oxygenation of the veins perturbs the magnetic field giving rise to localized phase shifts in a background of smoothly varying phase. Adapting the mixture

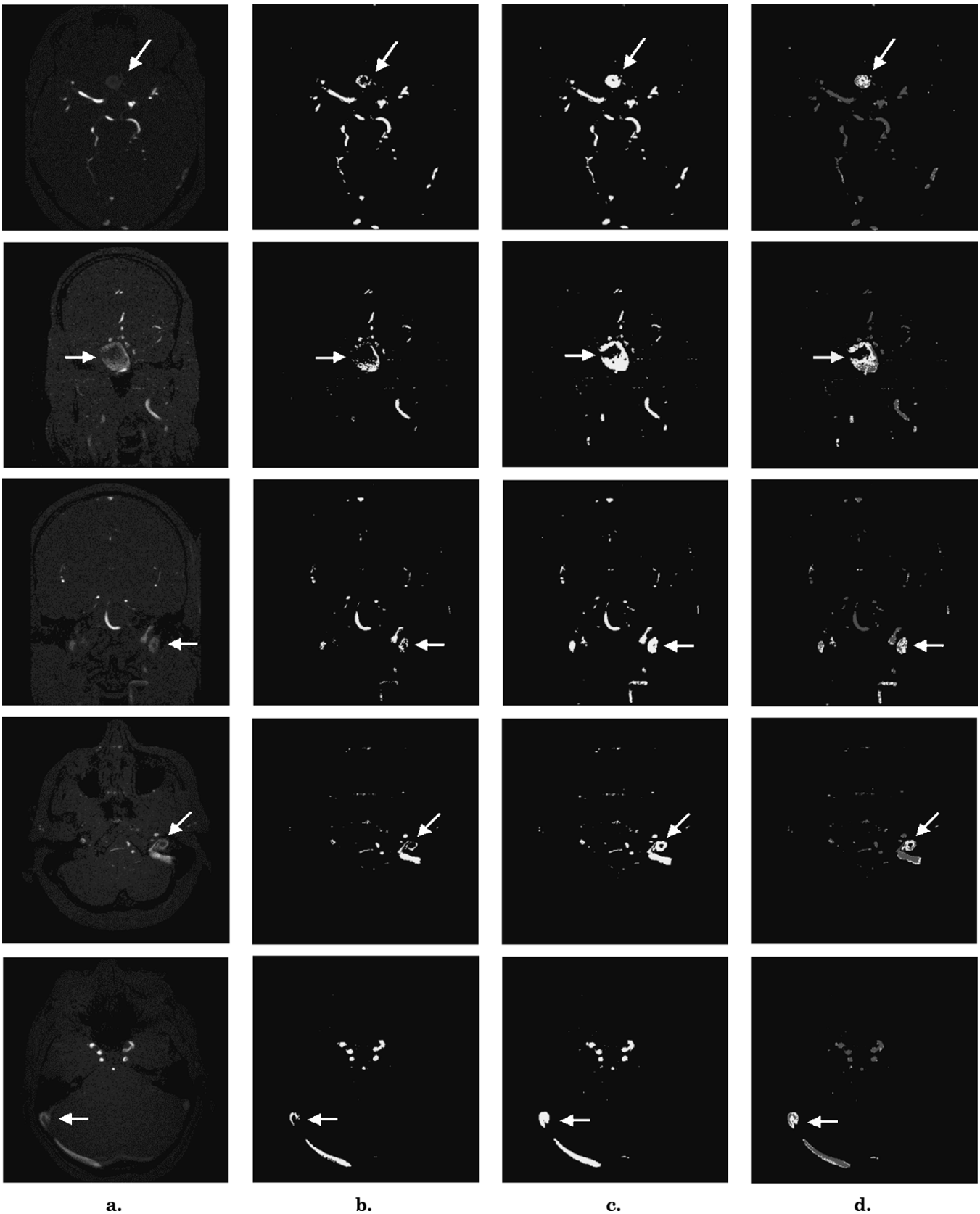

Fig. 14. Segmentation results and comparisons. (a) Original speed images. (b) Segmented images using speed information alone. (c) Segmented images using speed and flow coherence information. (d) The differences between (b) and (c) are white in color and the overlapping vessel regions are grey in color. The relatively low SNR and low flow rate regions, e.g., aneurysms and veins, are indicated by the arrows in the figures.

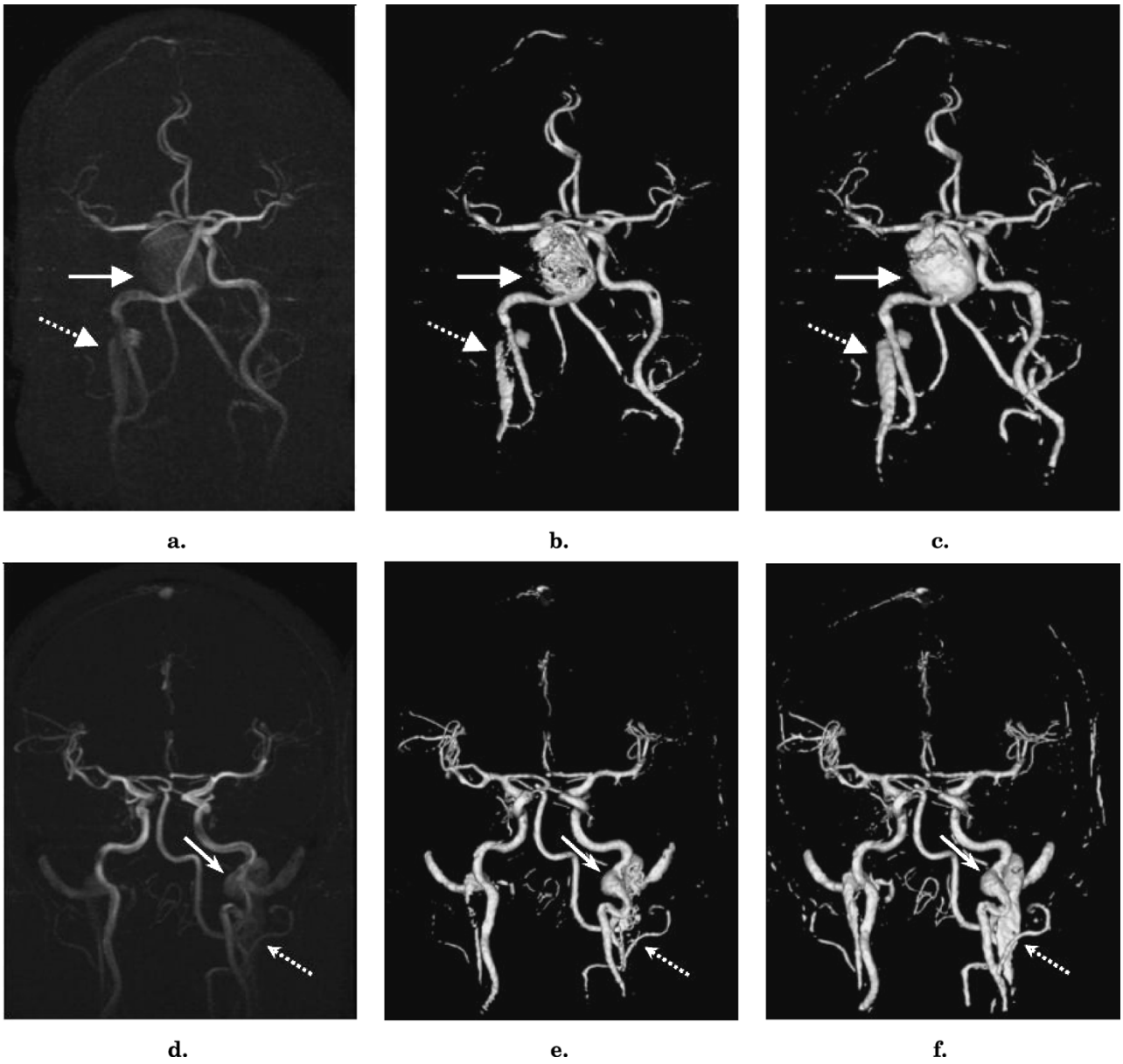

Fig. 15. Three-dimensional surfaces reconstructed based on the segmentation results. (a),(d) MIP. (b),(e) Three-dimensional surfaces of the segmentation results based on speed information alone. (c),(f) Three-dimensional surfaces of the segmentation results based on speed and flow coherence information. The relatively low SNR and low flow rate regions, e.g., aneurysms (solid) and veins (dashed), are indicated by the arrows in the figures.

model and perhaps reversing the phase coherence criteria may be of use in automatically and efficiently segmenting the veins in such images.

ACKNOWLEDGMENT

The authors would like to thank anonymous reviewers for the constructive comments. They are grateful to Dr. S. Yu at the Department of Diagnostic Radiology and Organ Imaging, Prince of Wales Hospital, Hong Kong, for his help in validation. A. C. S. Chung would like to thank Prof. M. Brady for his constructive comments throughout this work.

REFERENCES

[1] T. Lei and W. Sewchand, "Statistical approach to X-ray CT imaging and its applications in image analysis—I: A new stochastic model-based image segmentation technique for X-ray CT image," *IEEE Trans. Med. Imag.*, vol. 11, pp. 53–61, Mar. 1992.

[2] P. Santago and H. D. Gage, "Quantification of MR brain images by mixture density and partial volume modeling," *IEEE Trans. Med. Imag.*, vol. 12, pp. 566–574, Sept. 1993.

[3] Z. Liang, J. R. MaxFall, and D. P. Harrington, "Parameter estimation and tissue segmentation from multispectral MR images," *IEEE Trans. Med. Imag.*, vol. 13, pp. 441–449, Sept. 1994.

[4] J. C. Rajapakse, J. N. Giedd, and J. L. Rapoport, "Statistical approach to segmentation of single-channel cerebral MR images," *IEEE Trans. Med. Imag.*, vol. 16, pp. 176–186, Apr. 1997.

[5] K. Held, E. R. Kops, B. J. Krause, W. M. Wells III, R. Kikinis, and H. W. M. Gartner, "Markov random field segmentation of brain MR images," *IEEE Trans. Med. Imag.*, vol. 16, pp. 878–886, Dec. 1997.

[6] T. Kapur, "Model-based three-dimensional medical image segmentation," Ph.D. thesis, Artif. Intell. Lab., Massachusetts Inst. Technol., Cambridge, 1999.

[7] Y. Zhang, M. Brady, and S. Smith, "Segmentation of brain MR images through a hidden Markov random field model and the expectation-maximization algorithm," *IEEE Trans. Med. Imag.*, vol. 20, pp. 45–57, Jan. 2001.

[8] D. L. Wilson and J. A. Noble, "An adaptive segmentation algorithm for time-of-flight MRA data," *IEEE Trans. Med. Imag.*, vol. 18, pp. 938–945, Oct. 1999.

[9] A. C. S. Chung, J. A. Noble, and P. Summers, "Fusing speed and phase information for vascular segmentation of phase contrast MR angiograms," *Med. Image Anal.*, vol. 6, no. 2, pp. 109–128, 2002.

[10] A. C. S. Chung, "Vessel and aneurysm reconstruction using speed and flow coherence information in phase contrast magnetic resonance angiograms," D.Phil. thesis, Univ. Oxford, Oxford, U.K., 2001.

[11] J. McLachlan and D. Peel, *Finite Mixture Models*. New York: Wiley, 2000.

[12] T. McInerney and D. Terzopoulos, "Medical image segmentation using topologically adaptable surfaces," *Comput. Vis., Virtual Reality, Robot. Med.*, pp. 92–101, 1995.

[13] L. M. Lorigo, O. Faugeras, W. E. L. Grimson, R. Keriven, R. Kikinis, and C. F. Westin, "Co-dimension 2 geodesic active contours for MRA segmentation," in *Proc. Int. Conf. Information Processing in Medical Imaging*, 1999, pp. 126–139.

[14] O. Wink, W. J. Niessen, and M. A. Viergever, "Fast delineation and visualization of vessels in 3-D angiographic images," *IEEE Trans. Med. Imag.*, vol. 19, pp. 337–346, Apr. 2000.

[15] K. Krissian, G. Malandain, and N. Ayache, "Model-Based Detection of Tubular Structures in 3D Images," INRIA, Sophia Antipolis, France, Tech. Rep. 3736, 1999.

[16] H. J. Steiger Jr., J. N. Oshinski, R. I. Pettigrew, and D. N. Ku, "Computational simulation of turbulent signal loss in 2D time-of-flight magnetic resonance angiograms," *Magn. Reson. Med.*, vol. 37, pp. 609–614, 1997.

[17] D. J. Wilcock, T. Jaspan, and B. S. Worthington, "Problems and pitfalls of 3-D TOF magnetic resonance angiography of the intracranial circulation," *Clin. Radiol.*, vol. 50, pp. 526–532, 1995.

[18] P. A. Rinck, *Magnetic Resonance in Medicine*. Oxford, U.K.: Blackwell Scientific, 1993.

[19] C. Bishop, *Neural Networks for Pattern Recognition*. Oxford, U.K.: Clarendon, 1995.

[20] S. Kullback, *Information Theory and Statistics*. New York: Dover, 1997.

[21] R. M. Haralick, "Statistical and structural approaches to texture," *Proc. IEEE*, vol. 67, pp. 786–804, May 1979.

[22] R. M. Haralick, K. Shanmugam, and I. Dinstein, "Textural features for image classification," *IEEE Trans. Syst., Man, Cybern.*, vol. SMC-3, pp. 610–621, 1973.

[23] S. Geman and D. Geman, "Stochastic relaxation, Gibbs distributions, and the Bayesian restoration of images," *IEEE Trans. Pattern Anal. Machine Intell.*, vol. PAMI-6, pp. 721–741, June 1984.

[24] A. R. Rao and R. C. Jain, "Computerized flow field analysis: oriented texture fields," *IEEE Trans. Pattern Anal. Machine Intell.*, vol. 14, pp. 693–709, July 1992.

[25] P. Summers, A. Bhalerao, and D. Hawkes, "Multi-resolution, model-based segmentation of MR angiograms," *J. Magn. Reson. Med.*, vol. 7, no. 6, pp. 950–957, 1997.

[26] G. E. P. Box and G. C. Tiao, *Bayesian Inference in Statistical Analysis*. New York: Wiley, 1973.

[27] D. Geiger and F. Girosi, "Parallel and deterministic algorithms from MRFs: surface reconstruction," *IEEE Trans. Pattern Anal. Machine Intell.*, vol. 13, pp. 401–412, May 1991.

[28] F. Heitz and P. Bouthemy, "Multimodal estimation of discontinuous optical flow using Markov random fields," *IEEE Trans. Pattern Anal. Machine Intell.*, vol. 15, pp. 1217–1232, Dec. 1993.

[29] J. Besag, "On the statistical analysis of dirty pictures," *J. Roy. Statist. Soc., Series B (Methodological)*, vol. 48, no. 3, pp. 259–302, 1986.

[30] M. A. Bernstein, X. J. Zhou, J. A. Polzin, K. F. King, A. Ganin, N. J. Pelc, and G. H. Glover, "Concomitant gradient terms in phase contrast MR: analysis and correction," *Magn. Reson. Med.*, vol. 39, no. 2, pp. 300–308, 1998.

[31] M. E. Brummer, R. M. Mersereau, R. L. Eisner, and R. R. J. Lewine, "Automatic detection of brain contours in MRI data sets," *IEEE Trans. Med. Imag.*, vol. 12, pp. 152–166, June 1993.

[32] M. S. Atkins and B. T. Mackiewich, "Fully automatic segmentation of the brain in MRI," *IEEE Trans. Med. Imag.*, vol. 17, pp. 98–107, Feb. 1998.

[33] R. M. Henkelman, "Measurement of signal intensities in the presence of noise in MR images," *Med. Phys.*, vol. 12, no. 2, pp. 232–233, 1985.

[34] P. Summers, D. W. Holdsworth, H. Nikolov, Y. Papaharilou, and B. K. Rutt, "Design and construction of a robust flow phantom for the ISMRM flow and motion group multi-centre trial," in *Proc. Conf. Int. Soc. Magn. Reson. Med.*, 2000, p. 458.

[35] Y. C. Fung, *Biomechanics: Circulation*, 2nd ed. New York: Springer-Verlag, 1996.

[36] J. L. Helman and L. Hesselink, "Visualizing vector field topology in fluid flows," *IEEE Comput. Graphics Applicat.*, vol. 11, pp. 36–46, May. 1991.